Научном већу Института за физику у Београду

Београд, 21. 4. 2021.

Предмет: Прокретање поступка за избор у звање истраживач сарадник

Молим Научно веће Института за физику у Београду да покрене поступак за мој избор у звање истраживач сарадник.

У прилогу достављам:

1. мишљење руководиоца пројекта са предлогом комисије за избор у звање;

2. стручну биографију;

3. преглед научне активности;

4. списак и копије објављених научних радова и других публикација;

5. уверење о последњем овереном и уписаном семестру на докторским студијама;

6. фотокопију диплома са основних и мастер студија;

7. потврду о прихватању предлога теме докторске дисертације.

С поштовањем,

Ана Вранић,
истраживач приправник

Научном већу Института за физику у Београду

Предмет: Мишљење руководиоца лабораторије о избору Ане Вранић у звање истраживач сарадник

Ана Вранић је запослена у Лабораторији за примену рачунара у науци, у оквиру Националног центра изузетних вредности за изучавање комплексних система Института за физику у Београду. У истраживачком раду се бави проучавањем комплексних мрежа под руководством др Марије Митровић Данкулов. С обзиром да испуњава све предвиђене услове у складу са Правилником о стицању истраживачких и научних звања МПНТР, сагласан сам са покретањем поступка за избор Ане Вранић у звање истраживач сарадник.

За састав комисије за избор Ане Вранић у звање истраживач сарадник предлажем:

(1) др Марија Митровић Данкулов, виши научни сарадник, Институт за физику у Београду,
(2) др Александра Алорић, научни сарадник, Институт за физику у Београду,
(3) др Зорица Поповић, доцент Физичког факултета Универзитета у Београду.

др Антун Балаж
научни саветник
руководилац Лабораторије за
примену рачунара у науци

Биографија Ане Вранић

Ана Вранић је рођена 23.11.1993. године у Чачку, где је завршила основну школу и Гимназију. Након тога је уписала основне академске студије на Физичком факултету, универзитета у Београду, смер Теоријска и експериментална физика и дипломирала је 2016. године, са просечном оценом 9,24/10,00. Исте године уписује мастер академске студије на Физичком факултету, смер Теоријска и експериментална физика и завршава их 2017. године са просечном оценом 10,0. Мастер рад „Термодинамика и транспорт електрона у Хабардовом моделу на троугаоној решетки", је урађен под менторством др. Дарка Танасковића у оквиру Лабораторије за примену рачунара у науци Института за физику. У току летњег семестра Ана је посетила институт Јожеф Стефан у Љубљани у склопу израде мастер рада, при чему је била и стипендиста CEEPUS програма. Наредне године, добила је награду "Проф. др Љубомир Ћирковић" за најбољи мастер рад одбрањен на Физичком факултету у току протекле године.

Од новембра 2017. уписује докторске академске студије на Физичком факултету, смер физика кондензоване материје и статистичка физика. Под менторством Марије Митровић Данкулов, у оквиру Лабораторије за примену рачунара у науци Института за физику, научно истраживачки рад наставља на темама из статистичке физике комплексних система. Од априла 2018. године је запослена на Институту за физику, као истраживач приправник и ангажована на пројекту основних истраживања ОН171017 Моделирање и нумеричке симулације сложених вишечестичних система Министарства просвете, науке и технолошког развоја Републике Србије. Од септембра 2020. године је ангажована и на пројекту Artificial Intelligence Theoretical Foundations for Advanced Spatio-Temporal Modelling of Data and Processes (ATLAS), Фонда за науку Републике Србије.

До сада има два научна рада М21 категорије, као и саопштења са међународних скупова у изводу (М34). Своје резултате је приказала на неколико међународних конференција, од којих је најзаначајнија International Conference on Complex Networks and Their Applications, одржана у Лисабону 2019. године. Такође је била полазник школа за студенте докторских студија Spring Collage of Complex Systems у ICTP-у у Трсту (Италија), као и Complexity72h у Луки (Италија).

Преглед научне активности Ане Вранић

За време докторских студија, под руководством др Марије Митровић Данкулов, Ана Вранић се бави физиком комплексних система и изучавањем колективних феномена у многочестичним системима. Методи статистичке физике, као и методи комплексних мрежа се успешно могу применити на социо-економске системе што је довело до развоја области социо-физике. Током свог доктората Ана Вранић анализира структуру и раст социјалних мрежа у различитим онлајн и офлајн заједницама.

У стандардним моделима који описују еволуцију комплексних мрежа, подразумева се да мрежа расте линеарно. Међутим раст реалних заједница није константан у времену, па се као једно од важних питања намеће како неконстантан број нових чланова који се придружују систему може да измени структуру комплексне мреже. Број нових чланова се може представити сигналом. У објављеном раду, модел раста комплексних мрежа, који као параметре узима степен и старост чвора, је прилагођен како би се анализирали различити типови раста социјалних система. За разлику од Поасоновог сигнала у коме налазимо краткодометне корелације, код сигнала раста реалних заједница се срећу дугодометне кореалиције, мултифракталност, али и трендови који су типични за активност људи. У раду је показано да постоји критичан регион параметара модела где се јављају значајне разлике у повезаности међу чворовима, између мрежа насталих под утицајем побуде и константног сигнала, а том региону управо налазимо scale-free мреже. Мреже које су расле под утицајем побуде су кластерисане и корелисане за разлику од мрежа раслих константним сигналом. Такође на структуру мреже већи утицај имају сигнали са дугодометним корелацијама и мултифракталним особинама. Добијени резултати указују на то да у моделима раста комплексних мрежа сигнал раста представља важан параметар који би требало укључити при анализи комплексних мрежа.

Током мастер студија, под менторством др Дарка Танасковића, Ана Вранић се бавила изучавањем јако корелисаних система. Динамичка теорија средњег поља (Dynamical Mean-Field Theory - DMFT) је метод помоћу кога се могу описати јако-корелисани системи, заснива се на решавању модела нечистоће а нелокалне електронске корелације се занемарују. Међутим поставља се питање колико су нелокалне корелације битне за опис јако-корелисаних система. Анализиран је Хабардов модел на троугаоној решетки, коришћењем DMFT метода. Рачунате су проводне, термодинамиче, тако и транспортне особине електрона а резултати су потом поређени са резултатима коначно температурног Lanczos метода, који укључује нелокалне корелације. На вишим температурама нелокалне

корелације постају занемарљиве тако да не постоје ни разлике између DMFT и Lanczos резултата, док је на нижим температурама та разлика мала. Иако се троугаона решетка одликује магнетном фрустрацијом решетке, и сопствена енергија је више локализована, слични закључци се доносе и у случају квадрадне решетке. Са друге стране у раду је показано да допринос вертекс корекција у оптичкој проводности опстаје чак и на високим температурама за оба типа решетке.

Списак публикација Ане Вранић:

Радови у врхунским међународним часописима (категорија М21):

1. **A. Vranić** and M. Mitrović Dankulov,
   Growth signals determine the topology of evolving networks,
   J. Stat. Mech. 013405, (2021) [IF(2019)=2.215]
2. **A. Vranić**, J. Vučićević, J. Kokalj, J. Skolimowski, R. Žitko, J. Mravlje, and D. Tanasković,
   Charge Transport in the Hubbard Model at High Temperatures: Triangular Versus Square Lattice
   Phys. Rev. B 102, 115142 (2020) [IF(2019)=3.575]

Саопштења са међународног скупа штампана у изводу (категорија М34)

1. **A. Vranić** and M. Mitrović Dankulov, The role of driving signal in the evolution of social networks, The 8th International Conference on Complex Networks and Their Applications 10 - 12 December 2019, Lisbon, Portugal
2. A. Alorić, **A. Vranić**, M. Mitrović Dankulov and J. Smiljanić, Collective social phenomena: physics perspective, US - Serbia & West Balkan Data Science Workshop, 26-28 August 2018, Belgrade, Serbia
3. **A. Vranić** and M. Mitrović Dankulov, Social network structure: physics perspective, 4th Annual Meeting of COST Action TU1305 "Social Networks and Travel Behavior", 14-16 February 2018, Milan, Italy

Саопштење са скупа националног значаја штампано у изводу (категорија М64)

1. **A. Vranić** and M. Mitrović Dankulov, The influence of long-range correlated growth signals on the evolving complex network structures, Young Researcher's Conference 2020 - YOURS 2020

PAPER

Growth signals determine the topology of evolving networks

IOP ebooks™

Bringing together innovative digital publishing with leading authors from the global scientific community.

Start exploring the collection–download the first chapter of every title for free.

Growth signals determine the topology of evolving networks

Ana Vranić and Marija Mitrović Dankulov*

Institute of Physics Belgrade, University of Belgrade, Pregrevia 118, 11080
   Belgrade, Serbia
E-mail: anav@ipb.ac.rs and mitrovic@ipb.ac.rs

Abstract. Network science provides an indispensable theoretical framework for studying the structure and function of real complex systems. Different network models are often used for finding the rules that govern their evolution, whereby the correct choice of model details is crucial for obtaining relevant insights. Here, we study how the structure of networks generated with the aging nodes model depends on the properties of the growth signal. We use different fluctuating signals and compare structural dissimilarities of the networks with those obtained with a constant growth signal. We show that networks with power-law degree distributions, which are obtained with time-varying growth signals, are correlated and clustered, while networks obtained with a constant growth signal are not. Indeed, the properties of the growth signal significantly determine the topology of the obtained networks and thus ought to be considered prominently in models of complex systems.

Keywords: random graphs, networks, network dynamics, stochastic processes

S Supplementary material for this article is available online

Contents

*Author to whom any correspondence should be addressed.

1. Introduction

Emergent collective behavior is an indispensable property of complex systems [1]. It occurs as a consequence of interactions between a large number of units that compose a complex system, and it cannot be easily predicted from the knowledge about the behavior of these units. The previous research offers definite proof that the interaction network structure is inextricably associated with the dynamics and function of the complex system [2–9]. The structure of complex networks is essential for understanding the evolution and function of various complex systems [10–13].

The structure and dynamics of real complex systems are studied using complex network theory [1, 10, 11]. It was shown that real networks have similar topological properties regardless of their origins [14]. They have broad degree distribution, degree–degree correlations, and power-law scaling of clustering coefficient [11, 14]. Understanding how these properties emerge in complex networks leads to the factors that drive their evolution and shape their structure [2].

The complex network models substantially contribute to our understanding of the connection between the network topology and system dynamics and uncover underlying mechanisms that lead to the emergence of distinctive properties in real complex networks [15–17]. For instance, the famous Barabási–Albert model [15] finds the emergence of broad degree distribution to be a consequence of preferential attachment and network growth. Degree–degree anti-correlations of the internet can be explained, at least to a certain extent, by this constraint [18, 19]. Detailed analysis of the emergence of clustered networks shows that clustering is either the result of finite memory of the nodes [20] or occurs due to triadic closure [21].

Network growth, in combination with linking rules, shapes the network topology [22]. While various rules have been proposed to explain the topology of real networks [10], most models assume a constant rate of network growth, i.e., the addition of a fixed number of nodes at each time step [15, 20, 21]. However, empirical analysis of numerous technological and social systems shows that their growth is time-dependent [23–26]. The time-dependent growth of the number of nodes and links in the networks has been considered as a parameter in uncovering network growth mechanisms [27]. The accelerated growth of nodes in complex networks is the cause of the high heterogeneity in the distribution of web pages among websites [23] and the emergence of highly cited authors in citation networks [26]. The accelerated growth of the number of new links added in each time step changes the shape and scaling exponent of degree distribution

in the Barabási–Albert model [28] and model with preferential attachment with aging nodes [29].

The growth of real systems is not always accelerated. The number of new nodes joining the system varies in time, has trends, and exhibits circadian cycles typical for human behavior [24, 25, 30]. These signals are multifractal and have long-range correlations [31]. Some preliminary evidence shows that the time-varying growth influences the structure and dynamics of the social system and, consequently, the structure of interaction networks in social systems [25, 30, 32–34]. Still, which properties of the real growth signal have the most considerable influence, how different properties influence the topology of the generated networks, and to what extent is an open question.

In this work, we explore the influence of real and computer-generated time-varying growth signals on complex networks' structural properties. We adapt the aging nodes model [35] to enable time-varying growth. We compare the networks' structure using the growing signals from empirical data and randomized signals with ones grown with the constant signal using D-measure [36]. We demonstrate that the growth signal determines the structure of generated networks. The networks grown with time-varying signals have significantly different topology compared to networks generated through constant growth. The most significant difference between topological properties is observed for the values of model parameters for which we obtain networks with broad degree distribution, a common characteristic of real networks [10]. Our results show that real signals, with trends, cycles, and long-range correlations, alter networks' structure more than signals with short-range correlations.

This paper is divided as follows. In section 2, we provide a detailed description of growth signals. In section 3, we briefly describe the original model with aging nodes and structural properties of networks obtained for different values of model parameters [35]. We also describe the changes in the model that we introduce to enable time-varying growth. We describe our results in section 4 and show that the values of D-measure indicate large structural differences between networks grown with fluctuating and ones grown with constant signals. This difference is particularly evident for networks with power-law degree distribution and real growth signals. The networks generated with real signals are correlated and have hierarchical clustering, properties of real networks that do not emerge if we use constant growth. We discuss our results and give a conclusion in section 5.

2. Growth signals

The *growth signal* is the number of new nodes added in each time step. Real complex networks evolve at a different pace, and the dynamics of link creation define the time unit of network evolution. For instance, the co-authorship network grows through establishing a link between two scientists when they publish a paper [37]. In contrast, the links in an online social network are created at a steady pace, often interrupted by sudden bursts [38]. A paper's publication is thus a unit of time for the evolution of co-authorship networks, while the most appropriate time unit for social networks is 1 min or 1 h. While systems may evolve at a different pace, their evolution is often driven by the related mechanisms reflected by the similarity of their structure [10].
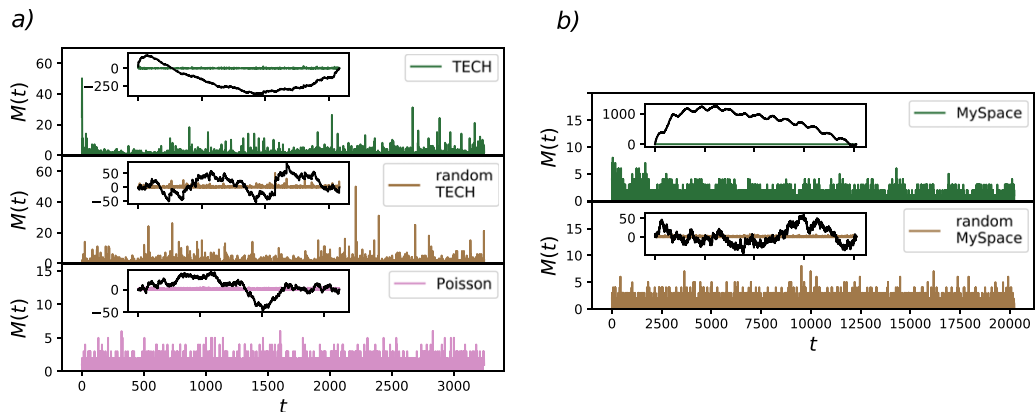
Figure 1. Growth signals for TECH (a) and MySpace (b) social groups, their randomized counterparts, and random signal drawn from Poissonian distribution with mean 1. The cumulative sums of signals' deviations from average mean value are shown in insets.

In this work, we use two different growth signals from real systems figure 1: (a) the data set from TECH community from Meetup social website [39] and (b) two months dataset of MySpace social network [40]. TECH is an event-based community where members organize offline events through the Meetup site [39]. The time unit for TECH is event since links are created only during offline group meetings. The growth signal is the number of people that attend the group's meetings for the first time. MySpace signal shows the number of new members occurring for the first time in the dataset [40] with a time resolution of 1 min. The number of newly added nodes for the TECH signal is $N = 3217$, and the length of the signal is $T_s = 3162$ steps. We have shortened the MySpace signal to $T_s = 20\,221$ time steps to obtain the network with $N = 10\,000$ nodes. The signals in the inset of figures 1(a) and (b) show the cumulative sum of deviations of signals from their average mean value, which is 1.017 for TECH and random TECH signal, 0.47 for MySpace and random MySpace, and 1 for Poissonian signal.

Real growth signals have long-range correlations, trends and cycles [25, 30, 40]. We also generate networks using randomized signals and one computer-generated white-noise signal to explore the influence of signals' features on evolving networks' structure. We randomize real signals using a reshuffling procedure. The reshuffling procedure consists of E steps. We randomly select two signal values at two distinct time steps and exchange their position in each step. The number of reshuffling steps is proportional to the length of the signal T_s, and in our case, it equals $100T_s$. Using this procedure, we keep the signal length and mean value, the number of added nodes, and the probability density function of fluctuations intact, but destroy cycles, trends, and long-range correlations. Besides, we generate a white-noise signal from a Poissonian probability distribution with a mean equal to 1. The length of the signal is $T = 3246$, and the number of added nodes in the final network is the same as for the TECH signal.

We characterize the long-range correlations of the growth signals calculating Hurst exponent [41, 42]. Hurst exponent describes the scaling behavior of time series $M(xt) = x^H M(t)$. It takes values between 0.5 and 1 for long-range correlated signals

and $H = 0.5$ for short-range correlated signals. The most commonly used method for estimating Hurst exponent of real, often non-stationary, temporal signals is detrended fluctuation analysis (DFA) [41]. The DFA removes trends and cycles of real signals and estimates Hurst exponent based on residual fluctuations. The DFA quantifies the scaling behavior of the second-moment fluctuations. However, signals can have deviations in fractal structure with large and small fluctuations that are characterized by different values of Hurst exponents [31].

We use multifractal detrended fluctuation analysis (MFDFA) [31, 43] to estimate multifractal Hurst exponent $H(q)$. For a given time series $\{x_i\}$ with length N, we first define global profile in the form of cumulative sum equation (1), where $\langle x \rangle$ represents an average of the time series:

$$Y(j) = \sum_{i=0}^{j} (x_i - \langle x \rangle), \quad j = 1, \ldots, N. \tag{1}$$

Subtracting the mean of the time series is supposed to eliminate global trends. Insets of figure 1 show global profiles of TECH, MySpace, their randomized signals and Poissonian distribution. The profile of the signal Y is divided into $N_s = \text{int}(N/s)$ non overlapping segments of length s. If N is not divisible with s the last segment will be shorter. This is handled by doing the same division from the opposite side of time series which gives us $2N_s$ segments. From each segment ν, local trend $p_{\nu,s}^m$—polynomial of order m—should be eliminated, and the variance $F^2(\nu, s)$ of detrended signal is calculated as in equation (2):

$$F^2(\nu, s) = \frac{1}{s} \sum_{j=1}^{s} \left[Y(j) - p_{\nu,s}^m(j) \right]^2. \tag{2}$$

Then the qth order fluctuating function is:

$$
\begin{aligned}
F_q(s) &= \left\{ \frac{1}{2N_s} \sum_{\nu}^{2N_s} \left[F^2(\nu, s) \right]^{\frac{q}{2}} \right\}^{\frac{1}{q}}, & q \neq 0 \\
F_0(s) &= \exp \left\{ \frac{1}{4N_s} \sum_{\nu}^{2N_s} \ln \left[F^2(\nu, s) \right] \right\}, & q = 0.
\end{aligned}
\tag{3}
$$

The fluctuating function scales as power-law $F_q(s) \sim s^{H(q)}$ and the analysis of log–log plots $F_q(s)$ gives us an estimate of multifractal Hurst exponent $H(q)$. Multifractal signal has different scaling properties over scales while monofractal is independent of the scale, i.e., $H(q)$ is constant.

Figures 1(a) and 2 show that the TECH signal has long trends and a broad probability density function of fluctuations. The trends are erased from the randomized TECH signal, but the broad distribution of the signal and average value remain intact. MFDFA analysis shows that real signals have long-range correlations with Hurst exponent approximately 0.6 for $q = 2$, figure 2. The TECH signal is multifractal, resulting from both broad probability distribution for the values of time series and different long-range correlations of the intervals with small and large fluctuations. Reshuffling of the
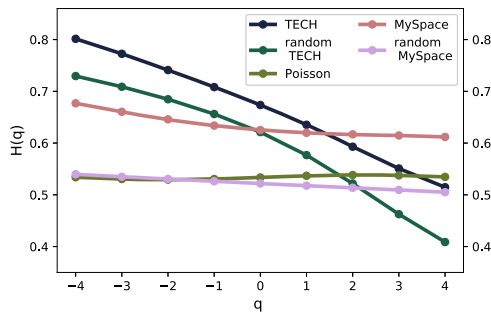
Figure 2. Dependence of Hurst exponent on parameter q for all five signals shown in figure 1 obtained with MFDFA.

time series does not destroy the broad distribution of values, which is the cause for the persistent multifractality of the TECH randomized signal is figure 2.

MySpace signal has a long trend with additional cycles that are a consequence of human circadian rhythm, figure 1(b). Circadian rhythm is an internal process that regulates the sleep-wake cycle and activity, and its period for humans is 24 h [44]. Circadian rhythm leads to periodic changes in online activity during the day and the emergence of a well-defined daily rhythm of activity that we see in figure 1(b). MySpace signal is multifractal for $q < 0$, and has constant value of $H(q)$ for $q > 0$, figure 2. In MFDFA, with negative values of q, we emphasize segments with smaller fluctuations, while for positive q, the emphasis is more on segments with larger fluctuations [43]. Segments with smaller fluctuations have more persistent long-range correlations in both real signals, see figure 2. Randomized MySpace signal and Poissonian signal are monofractal and have short-range with $H = 0.5$ correlations typical for white noise.

Detailed MDFA analysis of real, shuffled, and computer-generated signals are shown in figure S1 and table S1 of the supplementary material (https://stacks.iop.org/JSTAT/2021/013405/mmedia). In figure S1 we show in details how the $F_q(s)$ depends on s for different values of parameter q. The curve $F_q(s)$ exhibits different slopes for different values of q for multifractal signals, i.e., TECH, random TECH, and MySpace. $F_q(s)$ curves for monofractal signals are parallel. We provide the estimated values of $H(q)$ with estimated errors for q in a range from -4 to 4 for all five signals in table S1 of the supplementary material.

3. Model of aging nodes with time-varying growth

To study the influence of temporal fluctuations of growth signal on network topology, we need a model with linking rules where linking probability between network nodes depends on time. We use a network model with aging nodes [35]. In this model, the probability of linking the newly added node and the old one is proportional to their age difference and an old node's degree. In the original version of the model, one node is added to the network and linked to one old node in each time step. The old node is

chosen according to probability

$$\Pi_i(t) \sim k_i(t)^\beta \tau_i^\alpha \tag{4}$$

where $k_i(t)$ is a degree of a node i at time t, and τ_i is age difference between node i and newly added node. As was shown in [35], the values of model parameters β and α determine the topological properties of the resulting networks grown with the constant signal. According to this work, the networks generated using constant growth signals are uncorrelated trees for all values of model parameters. The phase diagram in α–β plain, obtained for $\beta > 0$ and $\alpha < 0$, shows that the degree distribution $P(k) \sim k^{-\gamma}$ with $\gamma = 3$ is obtained only along the line $\beta(\alpha^*)$, see [35] and figure S2 in the supplementary material. For $\alpha > \alpha^*$ networks have gel-like small world behavior, while for $\alpha < \alpha^*$ but close to line $\beta(\alpha^*)$ networks have stretched exponential shape of degree distribution [35].

Here we slightly change the original aging model [35] to enable the addition of more than one node and more than one link per newly added node in each time step. In each time step, we add $M \geqslant 1$ new nodes to the network and link them to $L \geqslant 1$ old nodes according to probability Π_i given in equation (4). Again, the networks with broad degree distribution are only generated for the combination of the model parameters along the critical line $\beta(\alpha^*)$. This line's position in the α–β plane changes with link density, while the addition of more than one node in each time step does not influence its position. Our analysis shows that the critical line's position is independent of the growth signal's properties, see figure S2 in the supplementary material showing phase diagram. For instance, for $L = 1$ networks and $\alpha = -1.25$ and $\beta = 1.5$ we obtain networks with power-law degree, while for $L = 2$ and $\beta = 1.5$ we need to increase the value of parameter α to -1.0 in order to obtain networks with broad degree distribution. Networks obtained for the values of model parameters $\beta(\alpha^*)$, $L \geqslant 2$, and constant growth have power-law degree distribution, are uncorrelated and have a finite non-zero value of clustering coefficient which does not depend on node degree, figure 4(b). If we fix the value of parameter β and lower down the value of parameter α to -1.5, the resulting networks are uncorrelated with a small value of clustering coefficient, see figure 4(a). For $\alpha < \alpha^*$ we obtain networks with stretched exponential degree distribution, without degree–degree correlations and small value of clustering exponent that does not depend on node degree (see figure S2 in the supplementary material). For $\alpha \ll \alpha^*$ the resulting networks are regular graphs. If we keep the value of α to 1.0 but increase the value β to 2.0 we enter the region of small world gels, see figure 4(c). The networks created for the values of $\alpha > \alpha^*$ are correlated networks with power-law dependence of the clustering coefficient on the degree (see figure S2 in the supplementary material). However, these networks do not have a power-law degree distribution.

The master equation approach is useful for studying the model with aging nodes when $M(t) = 1$ [45]. However, this approach is not sufficient for time-varying growth signals. In this work, we use numerical simulations to explore the case when $M(t)$ is a correlated time-varying function and study how these properties influence the structure of generated networks for different values of parameter $-\infty < \alpha \leqslant 0$ and $\beta \geqslant 1$ and constant L.

4. Structural differences between networks generated with different growth signals

We generate networks for different values of L, and different growth signal profiles $M(t)$. To examine how these properties influence the network structure, we compare the network structure obtained with different growth signals with networks of the same size grown with constant signal $M = 1$. The $M = 1$ is the closest constant value to average values of the signals, which are 1.017 for TECH, 0.47 for MySpace, and 1 for Poissonian signals. We explore the parameter space of the model by generating networks for pairs of values (α, β) in the range $-3 \leqslant \alpha \leqslant -0.5$ and $1 \leqslant \beta \leqslant 3$ with steps 0.5. For each pair of (α, β) we generated networks of different link density by varying parameter $L \in 1, 2, 3$, and for each combination of (α, β, L), we generate a sample of 100 networks and compare the structure of the networks grown with $M = 1$ with the ones grown with $M(t)$ shown in figure 1.

We quantify topological differences between two networks using D-measure defined in [36]

$$D(G, G') = \omega \left| \sqrt{\frac{J(P_1, \ldots, P_N)}{\log(d+1)}} - \sqrt{\frac{J(P'_1, \ldots, P'_N)}{\log(d'+1)}} \right| + (1 - \omega)\sqrt{\frac{J(\mu_G, \mu_{G'})}{log\,2}}. \quad (5)$$

D-measure captures the topological differences between two networks, G and G', on a local and global level. The first term in equation (5) evaluates dissimilarity between two networks on a local level. For each node in the network G one can define the distance distribution $P_i = \{p_i(j)\}$, where $p_i(j)$ is a fraction of nodes in network G that are connected to node i at distance j. The set of N node-distance distributions $\{P_1, \ldots, P_N\}$ contains a detailed information about network's topology. The heterogeneity of a graph G in terms of connectivity distances is measured through node network dispersion (NND). In [36] authors estimate NND as Jensen–Shannon divergence between N distance distributions $J(P_1, \ldots, P_N)$ normalized by $\log(d+1)$, where d is diameter of network G, and show that NND captures relevant features of heterogeneous networks. The difference between NNDs for graph G and G' captures the dissimilarity between the graph's connectivity distance profile.

However, certain graphs, such as k-regular graphs, have NND $= 0$ and can not be compared using NND. For these reasons, authors also introduce average node distance distribution of a graph $\mu(G) = \{\mu(1), \ldots, \mu(d)\}$, where $\mu(k)$ is the fraction of all pair of nodes in the network G that are at a distance k. The Jensen–Shannon divergence between $\mu(G)$ and $\mu(G')$ measures the difference between nodes' average connectivity in a graph G and G'. This term captures the differences between nodes on a global scale.

The original definition of D-measure also includes the third term, which quantifies dissimilarity in node α-centrality. The term can be omitted without precision loss [36]. The parameter ω in equation (5) determines the weight of each term. The extensive analysis shows that the choice $\omega = 0.5$ is the most appropriate for quantifying structural differences between two networks [36].

The D-measure takes the value between 0 and 1. The lower the value of D-measure is the more similar two networks are, with $D = 0$ for isomorphic graphs. The D-measure
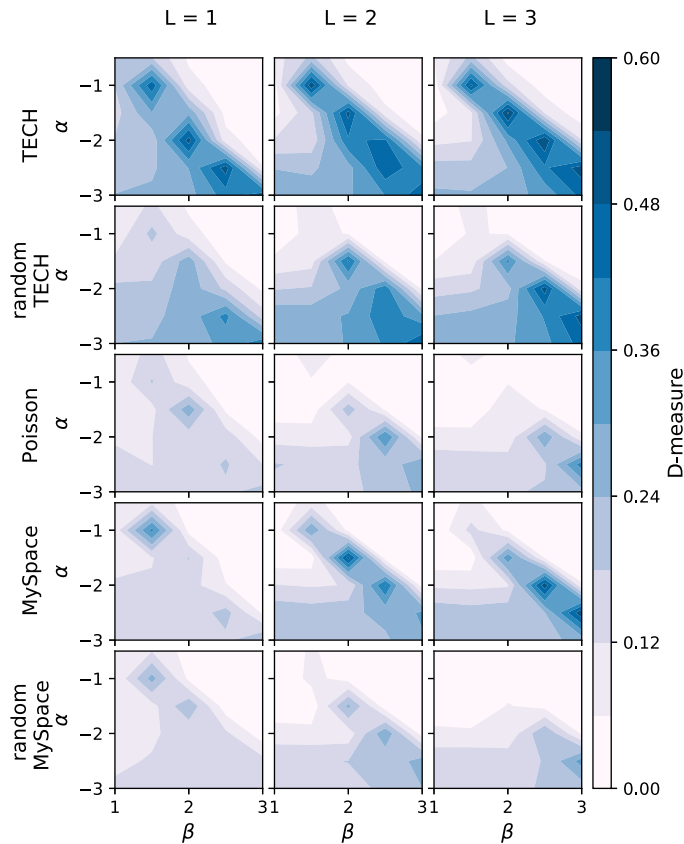
Figure 3. The comparison of networks grown with growth signals shown in figure 1 versus ones grown with constant signal $M = 1$, for value of parameter $\alpha \in [-3, -1]$ and $\beta \in [1, 3]$. $M(t)$ is the number of new nodes, and L is the number of links added to the network in each time step. The compared networks are of the same size.

outperforms previously used network dissimilarity measures such as Hamming distance and graph editing distance and clearly distinguishes between networks generated with the same model but with different values of model parameters [36].

For each pair of networks, one grown with constant and one with the fluctuating signal, we calculate the D-measure. The structural difference between networks grown with constant and fluctuating growth signal for fixed L and values of parameters α and β is obtained by averaging the D-measure calculated between all possible pairs of networks, see figure 3. We observe the non-zero value of D-measure for all time-varying signals. The D-measure has the largest value in the region around the line $\beta(\alpha^*)$. The values of D-measure in this region are similar to ones observed when comparing Erdös–Rényi graphs grown with linking probability below and above critical value [36]. For values $\beta < \beta(\alpha^*)$, the structural differences between networks grown with constant signal and $M(t)$ still exist, but they become smaller as we are moving away from the critical line. Networks obtained with constant signal and fluctuating signals have statistically similar structural properties in the region of small-world network gels, i.e., $\alpha > \alpha^*$.

We focus on the region around the critical line and observe the significant structural discrepancies between networks created for constant versus time-dependent growth signals for all signals regardless of their features. However, the value of D-measure depends on the signal's properties, figure 3. Networks grown with multifractal signals, TECH, random TECH, and MySpace signals, are the most different from those created by a constant signal. The D-measure has the maximum value for the original TECH signal, with $D_{\max} = 0.552$, the signal with the most pronounced multifractal properties among all signals shown in figure 2. Networks generated with randomized MySpace signal and Poisson signal are the least, but still notably dissimilar from those created with $M = 1$.

Randomized MySpace signal and Poissonian signal are monofractal signals with Hurst exponent $H = 0.5$. To investigate the influence of monofractal correlated signals on the network structure, we generate six signals with a different value of $H \in \{0.5, 0.6, 0.7, 0.8, 0.9, 1.0\}$, see figure S3 in the supplementary material. We use each of these signals to generate networks following the same procedure as for signals shown in figure 1. The results shown in figure S4 of the supplementary material confirm that short-range correlated signals create networks with different structures from ones grown with the constant signal. The increase of the Hurst exponent leads to increases in the D-measure. However, D-measure's maximal value is smaller than one observed for multifractal signals shown in figure 3.

The value of D-measure rises with a decline of α^*. This observation can be explained by examining linking rules and how model parameters determine linking dynamics between nodes. The ability of a node to acquire a link declines with its age and grows with its degree. A node's potential to become a hub, node with a degree significantly larger than average network degree, depends on the number of nodes added to the network in the T time steps after its birth. The length of the interval T decreases with parameter α. For constant signal, the number of nodes added during this time interval is constant and equal to MT. For fluctuating growth signals, the number of added nodes during the time T varies with time. In signals that have a broad distribution of fluctuations, like TECH signals, the peaks of the number of newly added nodes lead to the emergence of one or several hubs and super hubs. The emergence of super hubs, nodes connected to more than 30% of the nodes in the network, significantly alters the network's topology. For instance, super hubs' existence lowers the value of average path length and network diameter [10]. The emergence of hubs occurs for values of parameter α relative close to -1.0 for signals with long-range correlations. As we decrease the parameter α, the fluctuations present in the time-varying signals become more important, and we observe the emergence of hubs even for the white-noise signals. The trends present in real growth signals further promote the emergence of hubs. The impact of fluctuations and their temporal features on the structure of complex networks increases with link density.

The large number of structural properties observed in real networks are often consequences of particular degree distributions, degree correlations, and clustering coefficient [47]. Figure 4 shows the degree distribution $P(k)$, dependence of average neighboring degree on node degree $\langle k \rangle_{nn}(k)$, and dependence of clustering coefficient on node degree $c(k)$ for networks with average number of links per node $L = 2$. The significant structural differences between networks grown with real time-varying and constant signals
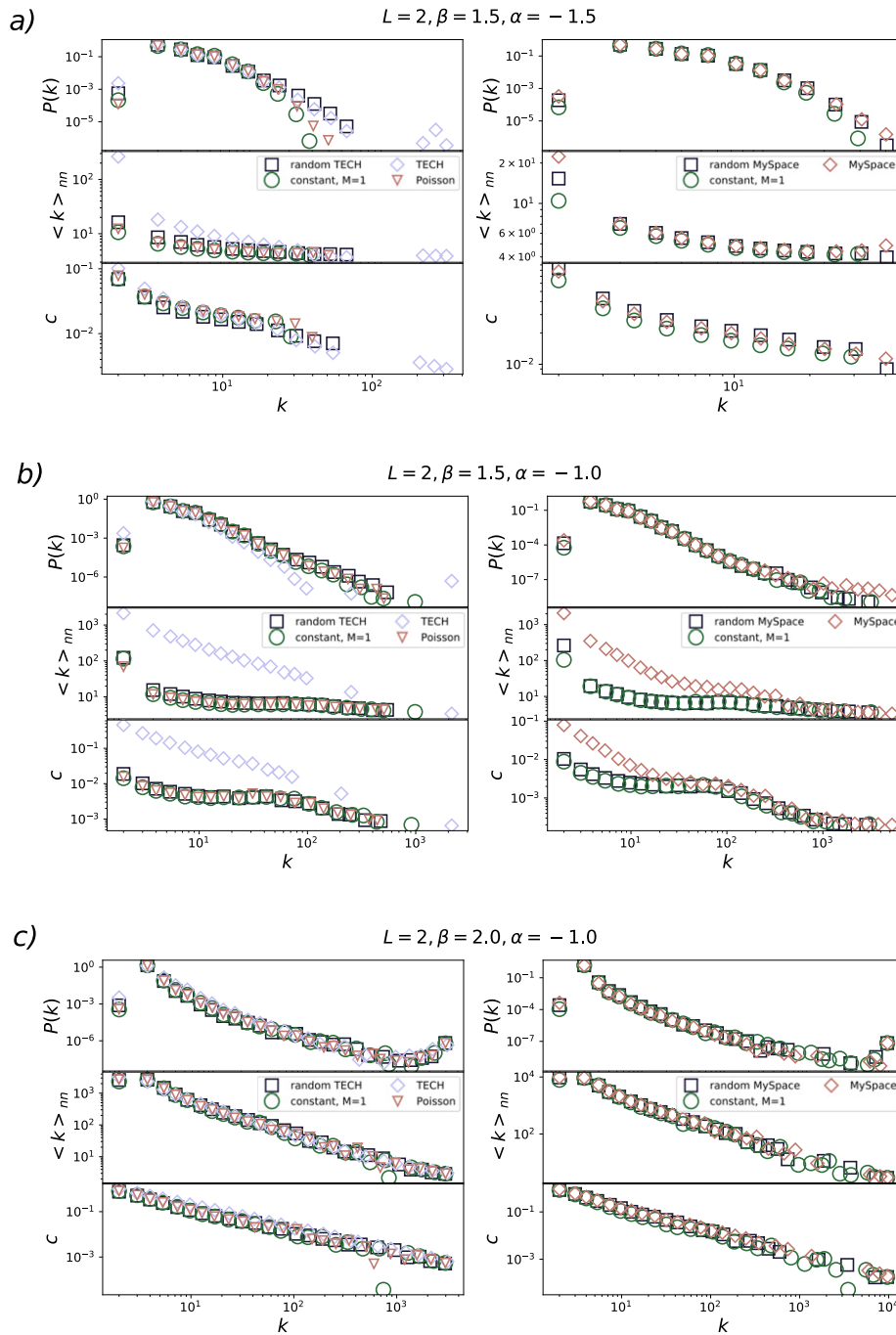
Figure 4. Degree distribution, the dependence of average first neighbor degree on node degree, dependence of node clustering on node degree for networks grown with different time-varying and constant signals. Model parameters have the values $\alpha = -1.5$, $\beta = 1.5$ (a), $\alpha = -1.0$, $\beta = 1.5$ (b), $\alpha = -1.0$, $\beta = 2.0$ (c), and $L = 2$ for all networks.

are observed for the values of model parameters $\alpha = -1.0$ and $\beta = 1.5$, figures 3 and 4(b). The degree distribution of networks generated for real signals shows the occurrence of super hubs in these networks. In contrast, degree distributions of networks generated with white-noise like signals do not differ from one created with constant signal, figure 4(b). Networks obtained for the real signals are disassortative and have a hierarchical structure, i.e., their clustering coefficient decreases with the degree. On the other hand, networks generated with constant and randomized signals are uncorrelated, and their clustering weakly depends on the degree.

We observe a much smaller, but still noticeable, difference between the topological properties of networks evolved with constant and time-varying signal for $\alpha < \alpha^*$, figure 4(a). The difference is particularly observable for degree distribution and dependence of average neighboring degree on node degree of networks grown with real TECH signal. The fluctuations of time-varying growth signals do not influence the topological properties of small-world gel networks, figure 4(c). For $\alpha > \alpha^*$, the super hubs emerge even with the constant growth. Since this is the mechanism through which the fluctuations alter the structure of evolving networks for $\alpha \lesssim \alpha^*$, the features of the growth signals cease to be relevant.

5. Discussion and conclusions

We demonstrate that the resulting networks' structure depends on the time-varying signal features that drive their growth. The previous research [25, 30] indicated the possible influence of temporal fluctuations on network properties. Our results show that growth signals' temporal properties generate networks with power-law degree distribution, non-trivial degree–degree correlations, and clustering coefficient even though the local linking rules, combined with constant growth, produce uncorrelated networks for the same values of model parameters [35].

We observe the most substantial dissimilarity in network structure along the critical line, the values of model parameters for which we generate broad degree distribution networks. Figure 3 shows that dissimilarity between networks grown with time-varying signals and ones grown with constant signals always exists along this line regardless of the features of the growth signal. However, the magnitude of this dissimilarity strongly depends on these features. We observe the largest structural difference between networks grown with multifractal TECH signal and networks that evolve by adding one node in each time step. The identified value of D-measure is similar to one calculated in the comparison between sub-critical and super-critical Erdös–Rényi graphs [36] indicating the considerable structural difference between these networks. Our findings are further confirmed in figure 4(b). The networks generated with signals with trends and long-range temporal correlations differ the most from those grown with the constant signal. Our results show that even white-noise type signals can generate networks significantly different from ones created with constant signal for low values of α^*.

Randomized and computer-generated signals do not have trends or cycles. Nevertheless, networks grown with these signals have a significantly different structure from ones grown with constant M. Our results demonstrate that growth signals' temporal

fluctuations are the leading cause for the structural differences between networks evolved with the constant and time-varying signal. We observe the smallest, but significant, difference between networks generated with constant M and monofractal signal with short-range correlations. As we increase the Hurst exponent, the value of the D-measure increases. The most considerable differences are observed for multifractal signals TECH, random TECH, and MySpace.

The value of D-measure declines as we move away from the critical line, figure 3. The primary mechanism through which the fluctuations influence the structure of evolved networks is the emergence of hubs and super hubs. For values of $\alpha \ll \alpha^*$, the nodes attache to their immediate predecessors creating regular networks without hubs. For $\alpha \lesssim \alpha^*$ graphs have stretched exponential degree distribution with low potential for the emergence of hubs. Still, multifractal signal TECH enables the emergence of hub even for the values of parameters for which we observe networks with stretched-exponential degree distribution in the case of constant growth figure 4(a). By definition, small-world gels generated for $\alpha > \alpha^*$ have super-hubs [35] regardless of the growth signal. Therefore the effects that fluctuations produce in the growth of networks do not come to the fore for values of model parameters in this region of $\alpha-\beta$ plane.

In this work, we focus on the role of the node growth signal in evolving networks' structure. However, real networks do not evolve only due to the addition of new nodes, but also through addition of new links [27–29, 38]. Furthermore, the deactivation of nodes [48] and the links [48] influence the evolving networks' structure. Each of these processes alone can result in a different network despite having the same linking rules. The next step would be to examine how different combinations of these processes influence the evolving networks' structure. For instance, in [28], authors have examined the influence of the time-dependent number of added links $L(t)$ on the Barabási–Albert networks' structure. They show that as long as the average value of time-dependent signal $\langle L(t) \rangle$ is independent of time, the generated networks have a similar structure as Barabási–Albert networks, and that the degree distribution depends strongly on the behavior of $\langle L(t) \rangle$. It would be interesting to examine how correlated $L(t)$ signals influence networks' structure with aging nodes, where the age of a node plays a vital role in linking between new and old nodes. Moreover, we expect that the combination of time-varying growth of the number of nodes and the number of links will significantly influence these networks' structure.

Evolving network models are an essential tool for understanding the evolution of social, biological, and technological networks and mechanisms that drive it [10]. The most common assumption is that these networks evolve by adding a fixed number of nodes in each time step [10]. So far, the focus on developing growing network models was on linking rules and how different rules lead to networks of various structural properties [10]. Growth signals of real systems are not constant [25, 30]. They are multifractal, characterised with long-range correlations [25], trends and cycles [40]. Research on temporal networks has shown that temporal properties of edge activation in networks and their properties can affect the dynamics of the complex system [12]. Our results imply that modeling of social and technological networks should also include non-constant growth. Its combination with local linking rules can significantly alter the structure of generated networks.

Acknowledgments

References

[1] Ladyman J, Lambert J and Wiesner K 2013 What is a complex system? *Euro J. Phil. Sci.* **3** 33

[2] Barrat A, Barthelemy M and Vespignani A 2008 *Dynamical Processes on Complex Networks* (Cambridge: Cambridge University Press)

[3] Pascual M *et al* 2006 *Ecological Networks: Linking Structure to Dynamics in Food Webs* (Oxford: Oxford University Press)

[4] Castellano C, Fortunato S and Loreto V 2009 Statistical physics of social dynamics *Rev. Mod. Phys.* **81** 591

[5] Gosak G, Markovič R, Dolenšek J, Rupnik M S, Marhl M, Stožer A and Perc M 2018 Network science of biological systems at different scales: a review *Phys. Life Rev.* **24** 118–35

[6] Arenas A, Díaz-Guilera A, Kurths J, Moreno Y and Zhou C 2008 Synchronization in complex networks *Phys. Rep.* **469** 93

[7] Boccaletti S, Almendral J A, Guan S, Leyva I, Liu Z, Sendiña-Nadal I, Wang Z and Zou Y 2016 Explosive transitions in complex networks' structure and dynamics: percolation and synchronization *Phys. Rep.* **660** 1

[8] Chen H, Zhang H and Shen C 2018 Double phase transition of the Ising model in core-periphery networks *J. Stat. Mech.* 063402

[9] Kuga K and Tanimoto J 2018 Impact of imperfect vaccination and defense against contagion on vaccination behavior in complex networks *J. Stat. Mech.* 113402

[10] Boccaletti S, Latora V, Moreno Y, Chavez M and Hwang D 2006 Complex networks: structure and dynamics *Phys. Rep.* **424** 175

[11] Newman M E J 2010 *Networks: An Introduction* (Oxford: Oxford University Press)

[12] Holme P and Saramäki J 2012 Temporal networks *Phys. Rep.* **519** 97

[13] Boccaletti S, Bianconi G, Criado R, Del Genio C I, Gómez-Gardeñes J, Romance M, Sendiña-Nadal I, Wang Z and Zanin M 2014 The structure and dynamics of multilayer networks *Phys. Rep.* **544** 1

[14] Barabási A-L 2009 Scale-free networks: a decade and beyond *Science* **325** 412

[15] Barabási A-L and Albert R 1999 Emergence of scaling in random networks *Science* **286** 509

[16] Tadić B 2001 Dynamics of directed graphs: the world-wide web *Physica* A **293** 273

[17] Mitrović M and Tadić B 2009 Spectral and dynamical properties in classes of sparse networks with mesoscopic inhomogeneities *Phys. Rev.* E **80** 026123

[18] Maslov S, Sneppen K and Zaliznyak A 2004 Detection of topological patterns in complex networks: correlation profile of the internet *Physica* A **333** 529

[19] Park J and Newman M E J 2003 Origin of degree correlations in the internet and other networks *Phys. Rev.* E **68** 026112

[20] Klemm K and Eguiluz V M 2002 Highly clustered scale-free networks *Phys. Rev.* E **65** 036123

[21] Serrano M A and Boguná M 2005 Tuning clustering in random networks with arbitrary degree distributions *Phys. Rev.* E **72** 036133

[22] Vázquez A 2003 Growing network with local rules: preferential attachment, clustering hierarchy, and degree correlations *Phys. Rev.* E **67** 056104

[23] Huberman B A and Adamic L A 1999 Growth dynamics of the world-wide web *Nature* **401** 131

[24] Mitrović M and Tadić B 2010 Bloggers behavior and emergent communities in blog space *Eur. Phys. J.* B **73** 293

[25] Dankulov M M, Melnik R and Tadić B 2015 The dynamics of meaningful social interactions and the emergence of collective knowledge *Sci. Rep.* **5** 1

[26] Liu J, Li J, Chen Y, Chen X, Zhou Z, Yang Z and Zhang C-J 2019 Modeling complex networks with accelerating growth and aging effect *Phys. Lett.* A **383** 1396

[27] Pham T, Sheridan P and Shimodaira H 2016 Joint estimation of preferential attachment and node fitness in growing complex networks *Sci. Rep.* **6** 32558

[28] Sen P 2004 Accelerated growth in outgoing links in evolving networks: deterministic versus stochastic picture *Phys. Rev.* E **69** 046107

[29] Dorogovtsev S N and Mendes J F F 2001 Effect of the accelerating growth of communications networks on their structure *Phys. Rev.* E **63** 025101

[30] Mitrović M and Tadić B 2012 *Emergence and Structure of Cybercommunities* (*Springer Optimization and Its Applications*) vol 57 (Berlin: Springer) p 209

[31] Kantelhardt J W, Zschiegner S A, Koscielny-Bunde E, Havlin S, Bunde A and Stanley H E 2002 Multifractal detrended fluctuation analysis of nonstationary time series *Physica* A **316** 87

[32] Mitrović M, Paltoglou G and Tadić B 2011 Quantitative analysis of bloggers' collective behavior powered by emotions *J. Stat. Mech.* P02005

[33] Tadić B, Dankulov M M and Melnik R 2017 Mechanisms of self-organized criticality in social processes of knowledge creation *Phys. Rev.* E **96** 032307

[34] Tadić B and Šuvakov M 2013 Can human-like bots control collective mood: agent-based simulations of online chats *J. Stat. Mech.* P10014

[35] Hajra K B and Sen P 2004 Phase transitions in an aging network *Phys. Rev.* E **70** 056103

[36] Schieber T A, Carpi L, Díaz-Guilera A, Pardalos P M, Masoller C and Ravetti M 2017 Quantification of network structural dissimilarities *Nat. Commun.* **8** 1

[37] Sarigöl E, Pfitzner R, Scholtes I, Garas A and Schweitzer F 2014 Predicting scientific success based on coauthorship networks *EPJ Data Sci.* **3** 9

[38] Myers S A and Leskovec J 2014 The bursty dynamics of the twitter information network *Proc. 23rd Int. Conf. on World Wide Web* 913

[39] Smiljanić J and Dankulov M M 2017 Associative nature of event participation dynamics: a network theory approach *PloS One* **12** e0171565

[40] Šuvakov M, Mitrovi M, Gligorijevi V and Tadi B 2013 How the online social networks are used: dialogues-based structure of MySpace *J. R. Soc. Interface* **10** 20120819

[41] Peng C-K, Buldyrev S V, Havlin S, Simons M, Stanley H E and Goldberger A L 1994 Mosaic organization of DNA nucleotides *Phys. Rev.* E **49** 1685

[42] Kantelhardt J W, Koscielny-Bunde E, Rego H H A, Havlin S and Bunde A 2001 Detecting long-range correlations with detrended fluctuation analysis *Physica* A **295** 441

[43] Fürst EAFI Ihlen E A 2012 Introduction to multifractal detrended fluctuation analysis in Matlab *Front. Physiol.* **3** 141

[44] Wever R A 2013 *The Circadian System of Man: Results of Experiments under Temporal Isolation* (Berlin: Springer)

[45] Dorogovtsev S N and Mendes J F F 2001 Scaling properties of scale-free evolving networks: continuous approach *Phys. Rev.* E **63** 056125

[46] Orsini C *et al* 2015 Quantifying randomness in real networks *Nat. Commun.* **6** 8627

[47] Tian L, Zhu C-P, Shi D-N, Gu Z-M and Zhou T 2006 Universal scaling behavior of clustering coefficient induced by deactivation mechanism *Phys. Rev.* E **74** 046103

[48] Gagen M J and Mattick J S 2005 Accelerating, hyperaccelerating, and decelerating networks *Phys. Rev.* E **72** 016123

Charge transport in the Hubbard model at high temperatures: Triangular versus square lattice

A. Vranić [1] J. Vučičević,[1] J. Kokalj,[2,3] J. Skolimowski,[3,4] R. Žitko,[3,5] J. Mravlje,[3] and D. Tanasković [1]

[1]*Institute of Physics Belgrade, University of Belgrade, Pregrevica 118, 11080 Belgrade, Serbia*
[2]*University of Ljubljana, Faculty of Civil and Geodetic Engineering, Jamova 2, Ljubljana, Slovenia*
[3]*Jožef Stefan Institute, Jamova 39, SI-1000 Ljubljana, Slovenia*
[4]*International School for Advanced Studies (SISSA), Via Bonomea 265, I-34136 Trieste, Italy*
[5]*University of Ljubljana, Faculty of Mathematics and Physics, Jadranska 19, Ljubljana, Slovenia*

High-temperature bad-metal transport has been recently studied both theoretically and in experiments as one of the key signatures of strong electronic correlations. Here we use the dynamical mean field theory and its cluster extensions, as well as the finite-temperature Lanczos method to explore the influence of lattice frustration on the thermodynamic and transport properties of the Hubbard model at high temperatures. We consider the triangular and the square lattices at half-filling and at 15% hole doping. We find that for $T \gtrsim 1.5t$ the self-energy becomes practically local, while the finite-size effects become small at lattice size 4×4 for both lattice types and doping levels. The vertex corrections to optical conductivity, which are significant on the square lattice even at high temperatures, contribute less on the triangular lattice. We find approximately linear temperature dependence of dc resistivity in doped Mott insulator for both types of lattices.

I. INTRODUCTION

Strong correlation effects in the proximity of the Mott metal-insulator transition are among the most studied problems in modern condensed matter physics. At low temperatures, material-specific details play a role, and competing mechanisms can lead to various types of magnetic and charge density wave order, or superconductivity [1–5]. At higher temperatures, physical properties become more universal, often featuring peculiarly high and linear-in-temperature resistivity (the bad-metal regime) [6–12] and gradual metal-insulator crossover obeying typical quantum critical scaling laws [13–17].

There are a number of theoretical studies of transport in the high-T regime based on numerical solutions of the Hubbard model [10,12,13,18,19], high-T expansion [20], and field theory [21–23]. Finding numerically precise results is particularly timely having in mind a very recent laboratory realization of the Hubbard model using ultracold atoms on the optical lattice [24]. This system enables fine tuning of physical parameters in a system without disorder and other complications of bulk crystals, which enables a direct comparison between theory and experiment. In our previous work (Ref. [25]) we have performed a detailed analysis of single- and two-particle correlation functions and finite-size effects on the square lattice using several complementary state-of-the-art numerical methods, and established that a finite-temperature Lanczos method (FTLM) solution on the 4×4 lattice is nearly exact at high temperatures. The FTLM, which calculates the correlation functions directly on the real-frequency axis, is recognized [25] as the most reliable method for calculating the transport properties of the Hubbard model at high temperatures. The dependence of charge transport and

thermodynamics on the lattice geometry has not been examined in Ref. [25] and it is the subject of this work.

Numerical methods that we use are (cluster) dynamical mean field theory (DMFT) and FTLM. The DMFT treats an embedded cluster in a self-consistently determined environment [26]. Such a method captures long-distance quantum fluctuations, but only local (in single-site DMFT), or short-range correlations (in cluster DMFT) [27]. The results are expected to converge faster with the size of the cluster than in the FTLM, which treats a finite cluster with periodic boundary conditions [28]. FTLM suffers from the finite-size effects in propagators as well as in correlations. The conductivity calculation in DMFT is, however, restricted just to the bubble diagram, while neglecting the vertex corrections. Approximate calculation of vertex corrections is presented in few recent works [29–34]. This shortcoming of DMFT is overcome in FTLM where one calculates directly the current-current correlation function which includes all contributions to the conductivity. Also, the FTLM calculates conductivity directly on the real-frequency axis, thus eliminating the need for analytical continuation from the Matsubara axis which can, otherwise, lead to unreliable results (see Supplemental Material of Ref. [25]). Both DMFT and FTLM methods are expected to work better at high temperatures [35] when single- and two-particle correlations become more local, and finite-size effects less pronounced. Earlier work has shown that the single-particle nonlocal correlations become small for $T \gtrsim t$ for both the triangular and the square lattices [25,36,37].

In this paper we calculate the kinetic and potential energy, specific heat, charge susceptibility, optical and dc conductivity in the Hubbard model on a triangular lattice and make a comparison with the square-lattice results. We consider strongly correlated regime at half-filling and at 15% hole doping. In

agreement with the expectations, we find that at high temperatures, $T \gtrsim 1.5t$, the nonlocal correlations become negligible and the results for thermodynamic quantities obtained with different methods coincide, regardless of the lattice type and doping. At intermediate temperatures, $0.5t \lesssim T \lesssim 1.5t$, the difference between DMFT and FTLM remains rather small. Interestingly, we do not find that the thermodynamic quantities are more affected by nonlocal correlations on the square lattice in this temperature range, although the self-energy becomes more local on the triangular lattice due to the magnetic frustration. On the other hand, the vertex corrections to optical conductivity remain important even at high temperatures for both lattice types, but we find that they are substantially smaller in the case of a triangular lattice. For the doped triangular and square lattice the temperature dependence of resistivity is approximately linear for temperatures where the finite-size effects become negligible and where the FTLM solution is close to exact.

The paper is organized as follows. In Sec. II we briefly describe different methods for solving the Hubbard model. Thermodynamic and charge transport results are shown in Sec. III, and conclusions in Sec. IV. The Appendix contains a detailed comparison of the DMFT optical conductivity obtained with different impurity solvers, a brief discussion of the finite-size effects at low temperatures, and an illustration of the density of states in different transport regimes.

II. MODEL AND METHODS

We consider the Hubbard model given by the Hamiltonian

$$H = -t \sum_{\langle i,j \rangle, \sigma} c^{\dagger}_{i\sigma} c_{j\sigma} + U \sum_i n_{i\uparrow} n_{i\downarrow} - \mu \sum_{i\sigma} n_{i\sigma}, \quad (1)$$

where t is the hopping between the nearest neighbors on either triangular or square lattice. $c^{\dagger}_{i\sigma}$ and $c_{i\sigma}$ are the creation and annihilation operators, U is the onsite repulsion, $n_{i\sigma}$ is the occupation number operator, and μ is the chemical potential. We set $U = 10t$, $t = 1$, lattice constant $a = 1$, $e = \hbar = k_B = 1$ and consider the paramagnetic solution for $p = 1 - n = 1 - \sum_\sigma n_\sigma = 0.15$ hole doping and at half-filling.

We use the FTLM and DMFT with its cluster extensions to solve the Hamiltonian. FTLM is a method based on the exact diagonalization of small clusters (4×4 in this work). It employs the Lanczos procedure to obtain approximate eigenstates and uses sampling over random starting vectors to calculate the finite-temperature properties from the standard expectation values [28]. To reduce the finite-size effects, we further employ averaging over twisted boundary conditions.

The (cluster) DMFT equations reduce to solving a (cluster) impurity problem in a self-consistently determined effective medium. We consider the single-site DMFT, as well as two implementations of cluster DMFT: cellular DMFT (CDMFT) [38,39] and dynamical cluster approximation (DCA) [27]. In DMFT the density of states is the only lattice-specific quantity that enters into the equations. In CDMFT we construct the supercells in the real space and the self-energy obtains short-ranged nonlocal components within the supercell. In DCA we divide the Brillouin zone into several patches and the number of independent components of the self-energy equals the number of inequivalent patches. The DCA results on 4×4 and
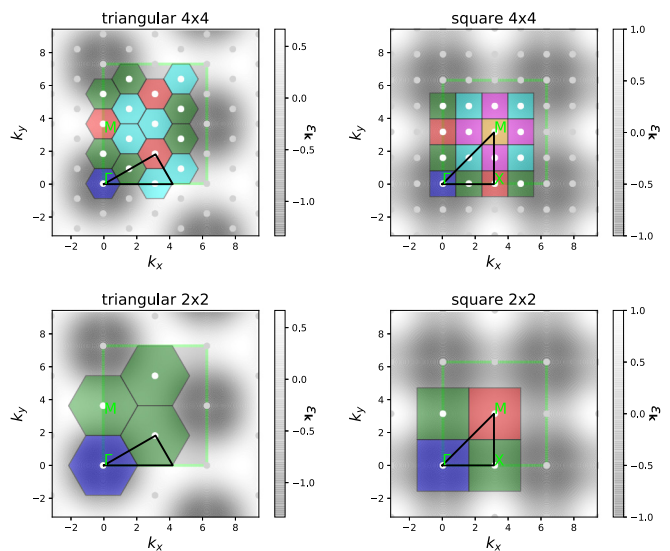

FIG. 1. DCA patches in the Brillouin zone. The irreducible Brillouin zone is marked by the black triangle. The dispersion relation is shown in gray shading. Note the position of the Γ point in the center of the first Brillouin zone which is not marked in this figure.

2×2 clusters are obtained by patching the Brillouin zone in a way that obeys the symmetry of the lattice, as shown in Fig. 1. As the impurity solver we use the continuous-time interaction expansion (CTINT) quantum Monte Carlo (QMC) algorithm [40,41]. In the single-site DMFT we also use the numerical renormalization group (NRG) impurity solver [42–45].

The (cluster) DMFT with QMC impurity solver (DMFT-QMC) gives the correlation functions on the imaginary (Matsubara) frequency axis, from which static quantities can be easily evaluated. The kinetic energy per lattice site is equal to

$$E_{\text{kin}} = \frac{1}{N} \sum_{\mathbf{k}} \varepsilon_{\mathbf{k}} n_{\mathbf{k}\sigma} = \frac{2}{N} \sum_{\mathbf{k}} \varepsilon_{\mathbf{k}} G_{\mathbf{k}}(\tau = 0^-), \quad (2)$$

where for the triangular lattice $\varepsilon_{\mathbf{k}} = -2t[\cos k_x + 2\cos(\frac{1}{2}k_x)\cos(\frac{\sqrt{3}}{2}k_y)]$ and for the square lattice $\varepsilon_{\mathbf{k}} = -2t(\cos k_x + \cos k_y)$ (gray shading in Fig. 1). The noninteracting band for the triangular lattice goes from $-6t$ to $3t$ with the van Hove singularity at $\varepsilon = t$. The potential energy is equal to

$$E_{\text{pot}} = Ud = \frac{1}{N} T \sum_{\mathbf{k}, i\omega_n} e^{i\omega_n 0^+} G_{\mathbf{k}}(i\omega_n) \Sigma_{\mathbf{k}}(i\omega_n), \quad (3)$$

where $d = \langle n_{i\uparrow} n_{i\downarrow} \rangle$ is the average double occupation. In DCA the cluster double occupation is the same as on the lattice, and we used the direct calculation of d in the cluster solver to cross check the consistency and precision of the numerical data. In CDMFT we calculated E_{pot} from periodized quantities G and Σ, where the periodization is performed on the self-energy and then the lattice Green's function is calculated from it. The total energy is $E_{\text{tot}} = E_{\text{kin}} + E_{\text{pot}}$. The specific heat $C = dE_{\text{tot}}/dT|_n$ is obtained by interpolating $E_{\text{tot}}(T)$ and then taking a derivative with respect to temperature. C is shown only in the DMFT solution where we had enough points

at low temperatures. The charge susceptibility $\chi_c = \partial n/\partial \mu$ is obtained from a finite difference using two independent calculations with μ that differs by a small shift $\delta\mu = 0.1t$. In the FTLM, C and χ_c are calculated without taking the explicit numerical derivative since the derivation can be done analytically from a definition of the expectation values,

$$C = C_\mu - \frac{T\zeta^2}{\chi_c}$$

$$= \frac{1}{N}\frac{1}{T^2}\left[\langle H^2 \rangle - \langle H \rangle^2 - \frac{(\langle HN_e \rangle - \langle H \rangle \langle N_e \rangle)^2}{\langle N_e^2 \rangle - \langle N_e \rangle^2}\right], \quad (4)$$

which is directly calculated in FTLM. Here, $C_\mu = \frac{1}{N}\frac{1}{T^2}[\langle(H-\mu N_e)^2\rangle - \langle H - \mu N_e\rangle^2]$, $\zeta = \frac{1}{N^2}\frac{1}{T^2}[\langle(H-\mu N_e)N_e\rangle - \langle H - \mu N_e\rangle\langle N_e\rangle]$, $\chi_c = \frac{1}{N}\frac{1}{T}(\langle N_e^2\rangle - \langle N_e\rangle^2)$, and $N_e = \sum_{i\sigma} n_{i\sigma}$ is the operator for the total number of electrons on the lattice.

We calculate the conductivity using DMFT and FTLM. Within the DMFT the optical conductivity is calculated from the bubble diagram as

$$\sigma(\omega) = \sigma_0 \iint d\varepsilon\, d\nu\, X(\varepsilon)A(\varepsilon,\nu)A(\varepsilon,\nu+\omega)$$

$$\times \frac{f(\nu) - f(\nu+\omega)}{\omega}, \quad (5)$$

where $X(\varepsilon) = \frac{1}{N}\sum_{\mathbf{k}}\left(\frac{\partial\varepsilon_k}{\partial k_x}\right)^2\delta(\varepsilon - \varepsilon_k)$ is the transport function, $A(\varepsilon,\nu) = -\frac{1}{\pi}\text{Im}[\nu + \mu - \varepsilon - \Sigma(\nu)]^{-1}$, and f is the Fermi function. For the square lattice $\sigma_0 = 2\pi$ and for triangular $\sigma_0 = 4\pi/\sqrt{3}$. For the calculation of conductivity in DMFT-QMC we need the real-frequency self-energy $\Sigma(\omega)$, which we obtain by Padé analytical continuation of the DMFT-QMC $\Sigma(i\omega_n)$. In the DMFT with NRG impurity solver (DMFT-NRG) we obtain the correlation functions directly on the real-frequency axis, but this method involves certain numerical approximations (see Appendix A).

In order to put into perspective the interaction strength $U = 10t$ and the temperature range that we consider, in Fig. 2 we sketch the paramagnetic (cluster) DMFT phase diagram for the triangular and square lattices at half-filling adapted from Refs. [46,47] (see also Refs. [36,37,48–54]). In the DMFT solution (blue lines) the critical interaction for the Mott metal-insulator transition (MIT) is $U_c \sim 2.5D$, where the half-bandwidth D is $4.5t$ and $4t$ for the triangular and the square lattice, respectively. The phase diagram features the region of coexistence of metallic and insulating solution below the critical end point at $T_c \approx 0.1t$. In this work we consider the temperatures above T_c. We set $U = 10t$, which is near U_c for the MIT in DMFT, but well within the Mott insulating part of the cluster DMFT and FTLM phase diagram.

III. RESULTS

We will first present the results for the thermodynamic properties in order to precisely identify the temperature range where the nonlocal correlations and finite-size effects are small or even negligible. In addition, from the thermodynamic quantities, e.g., from the specific heat, we can clearly identify the coherence temperature above which we observe the bad-metal transport regime. We then proceed with the key result
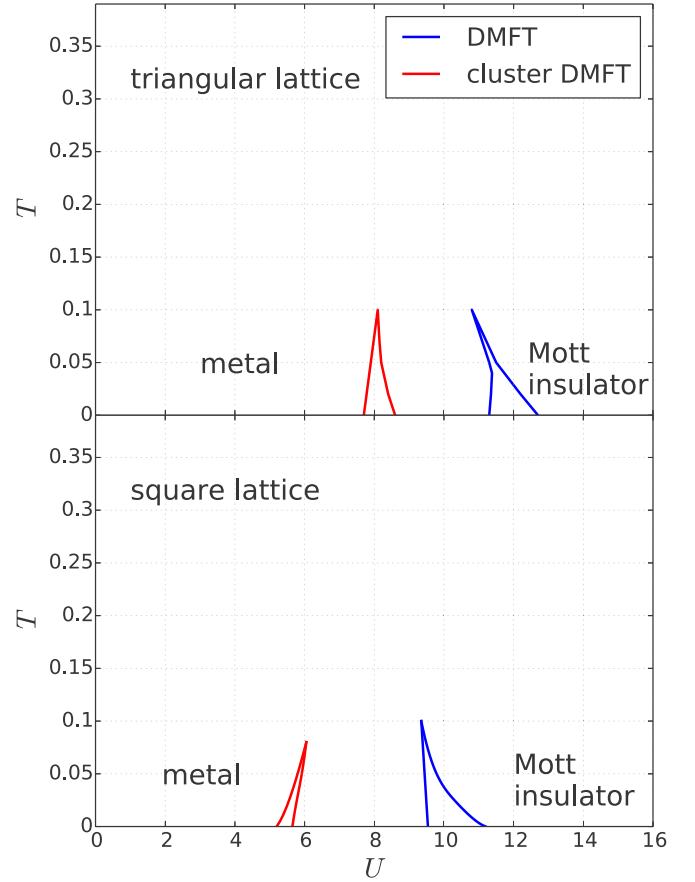

FIG. 2. Sketch of the paramagnetic phase diagram at half-filling, adapted from Refs. [46,47]. There is a region of the coexistence of metallic and insulating solution below the critical end point at T_c. The critical interaction is smaller in the cluster DMFT solution. Above T_c there is a gradual crossover from a metal to the Mott insulator. In this work we consider $T > T_c$ and $U = 10t$.

of this work by showing the contribution of vertex corrections to the resistivity and optical conductivity.

Before going into this detailed analysis, and in order to obtain a quick insight into the strength of nonlocal correlations, we compare in Fig. 3 the self-energy components in the cluster DMFT solution at two representative temperatures. We show the imaginary part of the DCA 4×4 self-energy at different patches of the Brillouin zone according to the color scheme of Fig. 1. The statistical error bar of the Im Σ results presented in Fig. 3 we estimate by looking at the difference in Im Σ between the last two iterations of the cluster DMFT loop. We monitor all $\mathbf{K}$ points and the lowest three Matsubara frequencies. At lower temperature (bottom row), this difference is smaller than 0.05 (0.01) for the square (triangular) lattice, respectively. At higher temperature (upper row), these values are both 10 times lower and the error bar is much smaller than the size of the symbol. At $T = 0.4t$ the differences in the self-energy components are more pronounced on the square than on the triangular lattice, which goes along the general expectations that the larger connectivity ($z = 6$) and the frustrated magnetic fluctuations lead to the more local self-energy. At $T \sim 1.5t$ all the components of the self-energy almost coincide for both lattices. We note that for the triangular
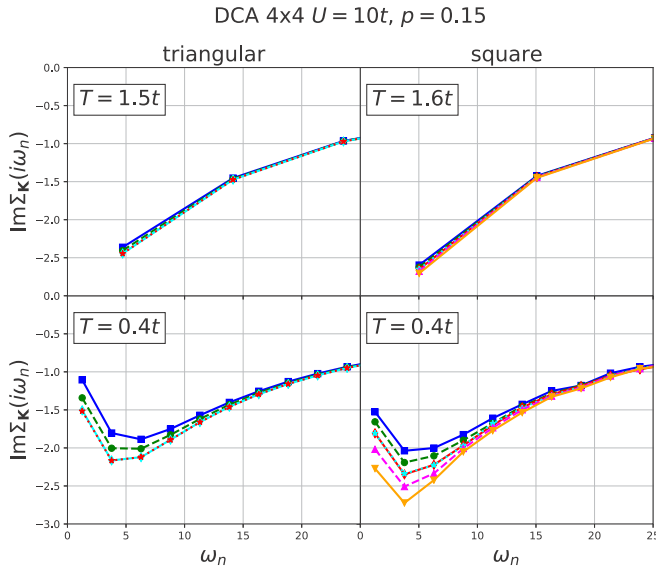
FIG. 3. Imaginary part of the self-energy at the Matsubara frequencies at different patches of the Brillouin zone for several temperatures for $p = 0.15$ hole doping. The position of the patches is indicated by the same colors as in Fig. 1. The solid lines are guide to the eye.

lattice the components of the self-energy marked by red and cyan colors are similar, but they do not coincide completely. There are four independent patches in this case. For the square lattice the red and cyan components of the self-energy are very similar, while we have six independent patches.

A. Thermodynamics

1. $p = 0.15$

We first show the results for hole doping $p = 0.15$. The results for the triangular lattice are shown in the left column of Fig. 4, and the results for the square lattice in the right column. Different rows correspond to the kinetic energy per lattice site E_{kin}, potential energy E_{pot}, total energy E_{tot}, specific heat $C = dE_{\mathrm{tot}}/dT|_n$, and charge susceptibility χ_c. The DMFT results are shown with blue solid lines and FTLM with red dashed lines. The red circles correspond to DCA 4×4, light green to DCA 2×2, green to CDMFT 2×2, and magenta to the CDMFT 2×1 result.

The FTLM results are shown down to $T = 0.2t$. The FTLM finite-size effects in thermodynamic quantities are small for $T \gtrsim 0.2t$ (see Appendix B). The DMFT results are shown for $T \geqslant 0.05t$ and cluster DMFT for $T \geqslant 0.2t$. Overall, the (cluster) DMFT and FTLM results for 15% doping look rather similar. The kinetic and potential energy do not differ much on the scale of the plots, and the specific heat looks similar.

The Fermi-liquid region, with $C \propto T$, is restricted to very low temperatures. For the triangular lattice we find a distinct maximum in $C(T)$ at $T \approx 0.4t$ in FTLM, and at $T \approx 0.3t$ in DMFT. This maximum is a signature of the coherence-incoherence crossover, when the quasiparticle peak in the density of states gradually diminishes and the bad-metal regime starts. The increase in the specific heat for $T \gtrsim 2t$ is
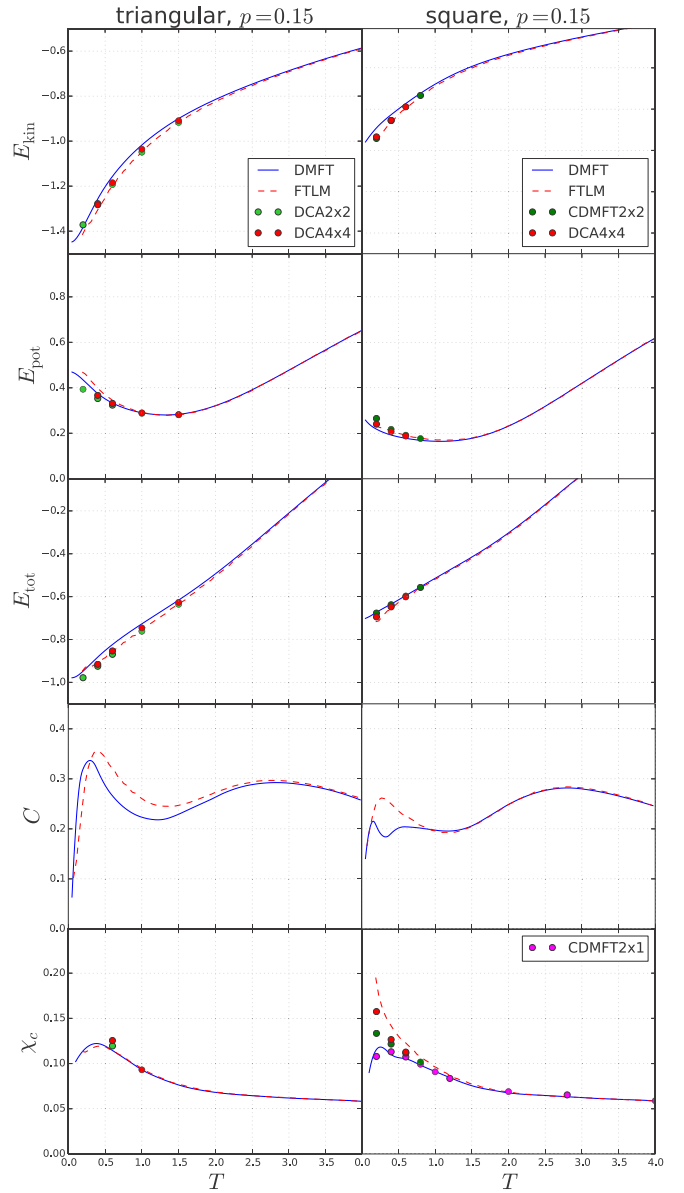

FIG. 4. Kinetic, potential, total energy, specific heat, and charge susceptibility as a function of temperature for the triangular and the square lattice at 15% doping.

caused by the charge excitations to the Hubbard band. The specific heat of the square lattice looks qualitatively the same. [A very small dip in the DMFT specific heat near $T = 0.4t$ for the square lattice may be an artifact of the numerics, where C is calculated by taking a derivative with respect to temperature of the interpolated $E_{\mathrm{tot}}(T)$.] We note that the specific heat, shown here for the fixed particle density, is slightly different than the one for the fixed chemical potential $C_\mu = dE_{\mathrm{tot}}/dT|_\mu$, as in Refs. [28,51,55].

For the square lattice all thermodynamic quantities obtained with different methods practically coincide for $T \gtrsim t$. This means that both the nonlocal correlations and the finite-size effects have negligible effect on thermodynamic quantities. For $T \lesssim t$ the DMFT and FTLM results start to differ. Interestingly, for the triangular lattice there is a small

difference in the DMFT and FTLM kinetic energy up to higher temperatures $T \sim 1.5t$. The FTLM and DCA 4×4 results coincide for $T \gtrsim t$, implying the absence of finite-size effects in the kinetic energy for both lattice types. We also note that the agreement of the CDMFT and DMFT solutions for the total energy on the square lattice at low temperatures is coincidental, as a result of a cancellation of differences in E_{kin} and E_{pot}.

The intersite correlations in the square lattice lead to an increase in the charge susceptibility at low temperatures (bottom panel in Fig. 4). Here, the FTLM and DCA 4×4 results are in rather good agreement. For the triangular lattice we found a sudden increase of χ_c at low temperatures in the DCA results (see Appendix B) but not in FTLM. These DCA points are not shown in Fig. 4 since we believe that they are an artifact of the particular choice of patching of the Brillouin zone. In order to keep the lattice symmetry, we had only four (in DCA 4×4) and two (in DCA 2×2) independent patches in the Brillouin zone for triangular lattice (Fig. 1). The average over twisted boundary conditions in FTLM reduces the finite-size error (see Appendix B), and hence we believe that the FTLM result for χ_c is correct down to $T = 0.2t$. We note that an increase of χ_c cannot be inferred from the ladder dual-fermion extension of DMFT [37] either. Still, further work would be needed to precisely resolve the low-T behavior of charge susceptibility for the triangular lattice.

2. $p = 0$

We now focus on thermodynamic quantities at half-filling (Fig. 5). In this case, the results can strongly depend on the method, especially since we have set the interaction to $U = 10t$, which is near the critical value for the Mott MIT in DMFT, while well within the insulating phase in the cluster DMFT and FTLM. The results with different methods almost coincide for $T \gtrsim 2t$ and are very similar down to $T \sim t$. The difference between the cluster DMFT and FTLM at half-filling is small, which means that the finite-size effects are small down to the lowest shown temperature $T = 0.2t$. Therefore, the substantial difference between the FTLM and single-site DMFT solutions at half-filling is mostly due to the absence of nonlocal correlations in DMFT.

The specific heat at half-filling is strongly affected by nonlocal correlations and lattice frustration. For triangular lattice the low-temperature maximum in $C(T)$ has different origin in the DMFT and FTLM solutions. The maximum in the FTLM is due to the low-energy spin excitations in frustrated triangular lattice, while in DMFT it is associated with the narrow quasiparticle peak since the DMFT solution becomes metallic as $T \to 0$. Our DMFT result agrees very well with the early work from Ref. [36] for $T \gtrsim t$. At lower temperatures there is some numerical discrepancy which we ascribe to the error due to the imaginary-time discretization in the Hirsch-Fye method used in that reference. For the square lattice the DMFT and FTLM solutions are both insulating. The maximum in the FTLM $C(T)$ is due to the spin excitations at energies $\sim 4t^2/U = 0.4t$, and it is absent in the paramagnetic DMFT solution which does not include dynamic nonlocal correlations. The increase in $C(T)$ at higher temperatures is due to the charge excitations to the upper Hubbard band.
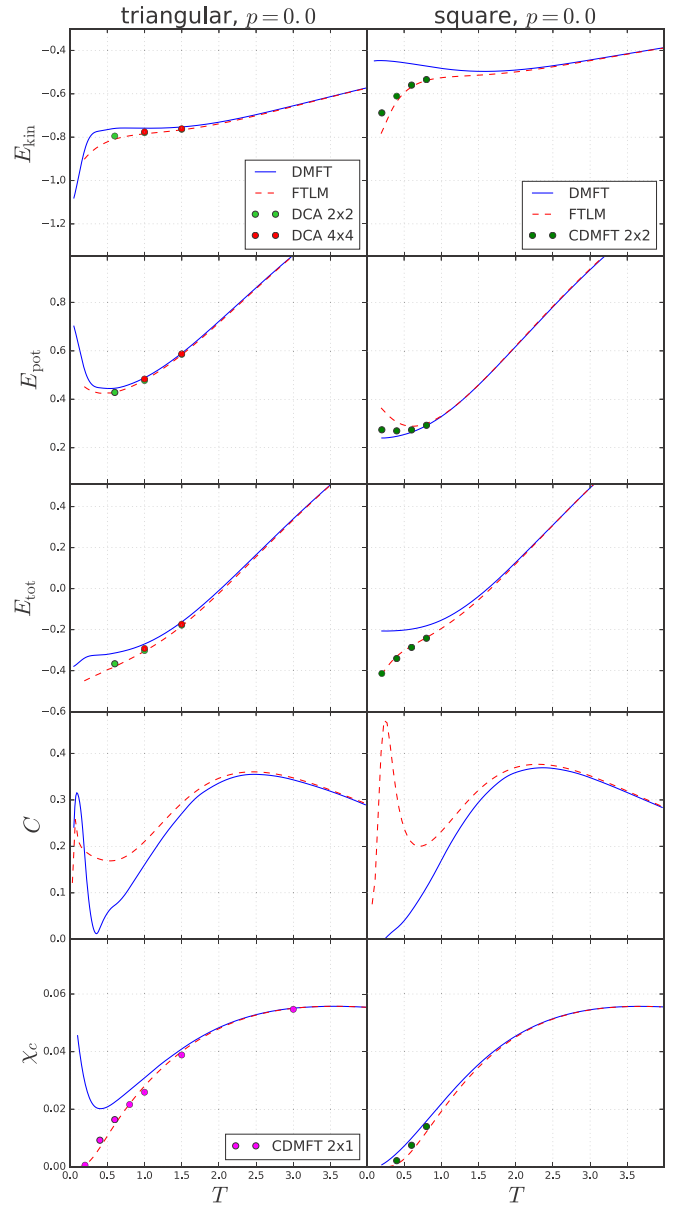

FIG. 5. Kinetic, potential, total energy, specific heat, and charge compressibility as a function of temperature for the triangular and the square lattice at half-filling.

B. Charge transport

The analysis of thermodynamic quantities has shown that the FTLM results for static quantities are close to exact down to $T \sim 0.5t$ or even $0.2t$. For charge transport we show the results for higher temperatures $T \gtrsim t$ since the finite-size effects are more pronounced in the current-current correlation function at lower temperatures.

An indication of the finite-size effects in optical conductivity can be obtained from the optical sum rule

$$\int_0^\infty d\omega\, \sigma(\omega) = \frac{\pi}{4V_{u.c.}}(-E_{\text{kin}}),\qquad (6)$$

where $V_{u.c}$ is equal to 1 and $\frac{\sqrt{3}}{2}$ for the square and triangular lattice, respectively. The deviation from the sum rule in FTLM
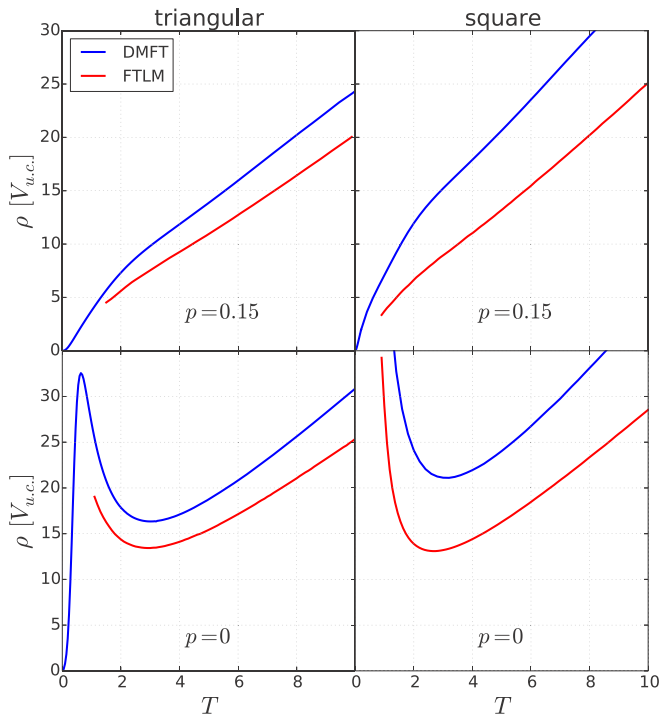
FIG. 6. Resistivity as a function of temperature.

FIG. 7. Optical conductivity at $T = 1.4$.

can be ascribed to the finite charge stiffness and δ function at zero frequency in optical conductivity [28]. The FTLM result for dc resistivity, shown by the red lines in Fig. 6, corresponds the temperature range where the weight of the δ-function peak at zero frequency (charge stiffness) [28] is smaller than 0.5% of the total spectral weight. The other finite-size effects are small and the FTLM resistivity is expected to be close to the exact solution of the Hubbard model. The remaining uncertainty, due to the frequency broadening, is estimated to be below 10% (see Supplemental Material in Ref. [25]). Smallness of the finite-size effects for the square lattice at $T \gtrsim t$ was also confirmed from the current-current correlation function calculated on the 4×4 and 8×8 lattices using CTINT QMC (see Ref. [25]). For doped triangular lattice we show the conductivity data for $T \gtrsim 1.5t$ since below this temperature the weight of the charge stiffness δ function is larger than 0.5% of the total weight, which indicates larger finite-size effects.

The DMFT resistivity is shown in Fig. 6 by the blue lines. It is obtained using the NRG impurity solver. Numerical error of the DMFT-NRG method is small, as we confirmed by a comparison with the DMFT-QMC calculation followed by the Padé analytical continuation (see Appendix A). We note that we do not show the conductivity data in the DCA since in this approximation we cannot reliably calculate the conductivity beyond the bubble term. At high temperatures the bubble-term contribution in cluster DMFT does not differ from the one in single-site DMFT since the self-energy becomes local [25].

Since the FTLM resistivity in Fig. 6 is shown only for temperatures when both the nonlocal correlations and the finite-size effects are small, the difference between the DMFT and FTLM resistivity is due to the vertex corrections. Their contribution corresponds to the connected part of the current-current correlation function whereas the DMFT conductivity
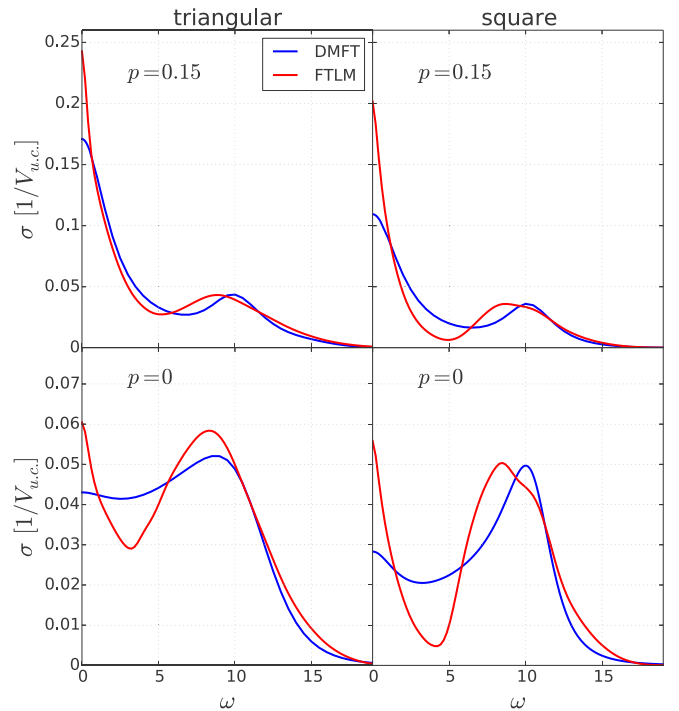
is given by the bubble diagram. A detailed analysis of vertex corrections for the square lattice is given in our previous work (Ref. [25]). Here, our main focus is on the comparison of the importance of vertex corrections for different lattices: the numerical results show that the vertex corrections to conductivity are less important in the case of the triangular lattice.

In the doped case, the FTLM solution gives the resistivity which is approximately linear in the entire temperature range shown in Fig. 6. This bad-metal linear-T temperature dependence is one of the key signatures of strong electronic correlations. The resistivity is here above the Mott-Ioffe-Regel limit which corresponds to the scattering length one lattice spacing within the Boltzmann theory. The Mott-Ioffe-Regel limit can be estimated as [6] $\rho_{\mathrm{MIR}} \sim \sqrt{2\pi} \approx 2.5$.

At half-filling and low temperatures the result qualitatively depends on the applied method. For the half-filled triangular lattice at $U = 10t$ the DMFT solution gives a metal, whereas the nonlocal correlations lead to the Mott insulating state. Still, similar as for thermodynamic quantities, the numerically cheap DMFT gives an insulatinglike behavior and a rather good approximation down to $T \sim 0.5t$.

The optical conductivity, shown in Fig. 7 for $T = 1.4t$, provides further insight into the dependence of the vertex correction on the lattice geometry. The DMFT-QMC conductivity is calculated using Eq. (5) with $\Sigma(\omega)$ obtained by the Padé analytical continuation of $\Sigma(i\omega_n)$ (see Appendix A for a comparison with DMFT-NRG). In the DMFT solution, the Hubbard peak is determined by the single-particle processes and it is centered precisely at $\omega = U$. The vertex corrections in FTLM shift the position of the Hubbard peak to lower frequencies. The total spectral weight is the same in FTLM and DMFT solution since it obeys the sum rule of Eq. (6), while the kinetic energies coincide. The Ward identity for

vertex corrections [25,31]

$$\Lambda^{\mathrm{conn}}(i\nu = 0) = -2T\frac{1}{N}\sum_{\mathbf{k}} v_{\mathbf{k}}\sum_{i\omega_n} G_{\mathbf{k}}^2(i\omega_n)\partial_{k_x}\Sigma_{\mathbf{k}}(i\omega_n) \quad (7)$$

also implies that the vertex corrections do not affect the sum rule if the self-energy is local. Here, $\Lambda(i\nu)$ is the current-current correlation function and $\Lambda(i\nu = 0) = \frac{1}{\pi}\int d\omega\,\sigma(\omega)$.

The results clearly show the much stronger effect of vertex corrections on the square lattice on all energy scales. In addition to a very different $\omega \to 0$ (dc) limit, we observe the more significant reduction of the Drude-like peak width and a larger shift of the Hubbard peak on the square lattice, with a more pronounced suppression of the optical weight at intermediate frequencies. We note that a broad low-frequency peak in conductivity is due to incoherent short-lived excitations characteristic of the bad-metal regime. The structure of the density of states in different transport regimes is discussed in Appendix C.

IV. CONCLUSION

In summary, we have performed a detailed comparison of the thermodynamic and charge transport properties of the Hubbard model on a triangular and square lattice. We identified the temperatures when the finite-size effects become negligible and the FTLM results on the 4×4 cluster are close to exact. In the doped case, for both lattice types, the resistivity is approximately linear in temperature for $T \gtrsim 1.5t$. In particular, we found that the contribution of vertex corrections to the optical and dc conductivity is smaller in the case of a triangular lattice, where it leads to ∼20% decrease in dc resistivity as compared to the bubble term. The vertex corrections also leave a fingerprint on the position of the Hubbard peak in the optical conductivity, which is shifted from $\omega = U$ to slightly lower frequencies.

On general grounds, higher connectivity and/or magnetic frustration should lead to more local self-energy and smaller vertex corrections in the case of triangular lattice, as it is observed. However, the precise role of these physical mechanisms and possible other factors remains to be established. Another important open question is to find an efficient approximate scheme to evaluate the vertex corrections, which would be sufficiently numerically cheap to enable calculations of transport at lower temperatures and in real materials. These issues are to be addressed in the future, but we are now better positioned as we have established reliable results that can serve as a reference point.

With this work we also made a benchmark of several state-of-the-art numerical methods for solving the Hubbard model and calculating the conductivity at high temperatures. This may be a useful reference for calculations of conductivity using a recent approach that calculates perturbatively the correlation functions directly on the real-frequency axis [56–59], thus eliminating a need for analytical continuation, while going beyond the calculation on the 4×4 cluster.

APPENDIX A: COMPARISON OF THE DMFT-NRG AND DMFT-QMC CONDUCTIVITY

Here, we compare the DMFT results for the dc resistivity and optical conductivity obtained with two different impurity solvers. The optical conductivity $\sigma(\omega)$ is calculated according to Eq. (5). The dc resistivity is equal to $\rho = \sigma^{-1}(\omega \to 0)$.

Within DMFT-NRG solver the self-energy is obtained directly on the real-frequency axis. There are three sources of errors in this approach: discretization errors, truncation errors, and (over)broadening errors. The method is based on the discretization of the continuum of states in the bath; the ensuing discretization errors can be reduced by performing the calculation for several different discretization meshes with interleaved points and averaging these results. It has been shown [45] that in the absence of interactions, the discretization error can be fully eliminated in a systematic manner. For an interacting problem, the cancellation of artifacts is only approximate, but typically very good, so that this is a minor source of errors. The truncation errors arise because in the iterative diagonalization one discards high-energy states after each set of diagonalizations. For static quantities this error is negligible, but it affects the dynamical (frequency-resolved) quantities because they are calculated from contributions linking kept and discarded states [61–63]. Finally, the raw spectral function in the form of δ peaks needs to be broadened in order to obtain the smooth spectrum. If the results are overbroadened, this can result in a severe overestimation of resistivity, and this is typically the main source of error in the NRG for this quantity. Fortunately, the resistivity is calculated as an integrated quantity, thus, the broadening kernel width can be systematically reduced [20,64]. The lower limit is set by the possible convergence issues in the DMFT self-consistency cycle due to jagged aspect of all quantities, where the actual limit value is problem dependent. In the NRG results reported in this work, it was possible to use very narrow broadening kernel. By studying the dependence of the $\rho(T)$ curves on the kernel width, we estimate that the presented results have at most a few percent error even at the highest temperatures considered.

The DMFT-QMC gives the self-energy $\Sigma(i\omega_n)$ at the Matsubara frequencies and the analytical continuation is necessary to obtain $\Sigma(\omega)$. The statistical error in QMC makes the analytical continuation particularly challenging. However, at high temperatures the CTINT QMC algorithm is very efficient. Running a single DMFT iteration for 10 minutes on 128 cores and using 20 or more iterations, we obtained the self-energies with the statistical error $|\delta\Sigma(i\omega_0)| \approx 5\times10^{-4}$ and $|\delta G(i\omega_0)| \approx 2\times10^{-5}$ at the first Matsubara frequency at $T = t$. Such a small statistical error makes the Padé analytical continuation possible for temperatures $T \lesssim 2t$.
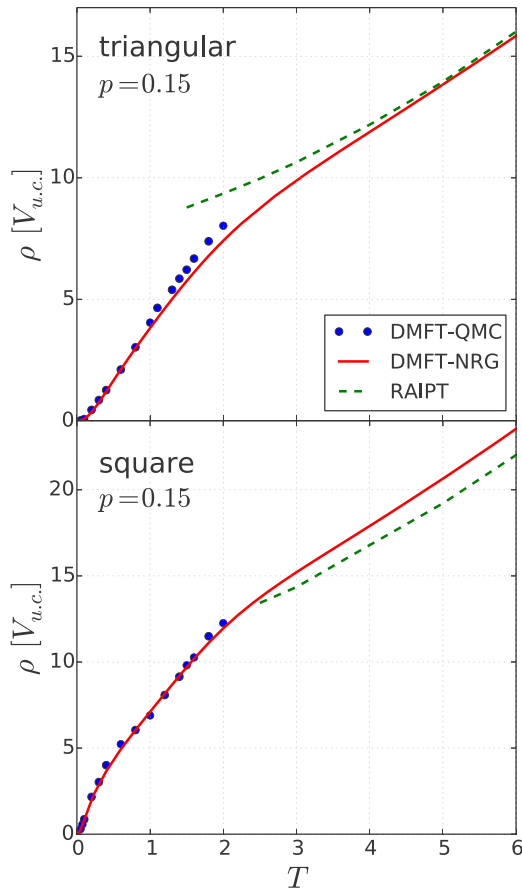
FIG. 8. DMFT-QMC (blue dots) and DMFT-NRG (red lines) resistivity as a function of temperature. The analytical continuation of the self-energy is performed with the Padé method. At high temperatures the DMFT-NRG result agrees rather well with the RAIPT (green dashed lines).

We have checked that Padé continuation gives similar results for $\Sigma(\omega)$ when performed on $\Sigma(i\omega_n)$ taken from last few DMFT iterations. We than used $\Sigma(i\omega_n)$ averaged over the last five iterations to further reduce the noise in $\Sigma(i\omega_n)$, before performing the Padé analytical continuation subsequently used in the calculation of the conductivity. We also obtained $G(\omega)$ directly by the Padé analytical continuation of $G(i\omega_n)$, and checked that the result is consistent with the one calculated as $G(\omega) = \int d\varepsilon\, \rho_0(\varepsilon)[\omega + \mu - \varepsilon - \Sigma(\omega)]^{-1}$. These cross checks have confirmed that Padé analytical continuation is rather reliable.

Figure 8 shows the temperature dependence of resistivity calculated with the DMFT-NRG (red lines) and DMFT-QMC (blue dots). For the square lattice we find excellent agreement between the two methods. For the triangular lattice we find some discrepancy for $T \sim 1.5t$, which is likely due to the approximations in DMFT-NRG. We also find that the real-axis iterative perturbation theory [65–67] (RAIPT) agrees rather well with the DMFT-NRG solution for $T \gtrsim 2t$.

It is also interesting to note how the lattice geometry can influence the range of the Fermi liquid $\rho \propto T^2$ behavior in the DMFT solution. In the DMFT equations the lattice structure enters only through the noninteracting density of states. We
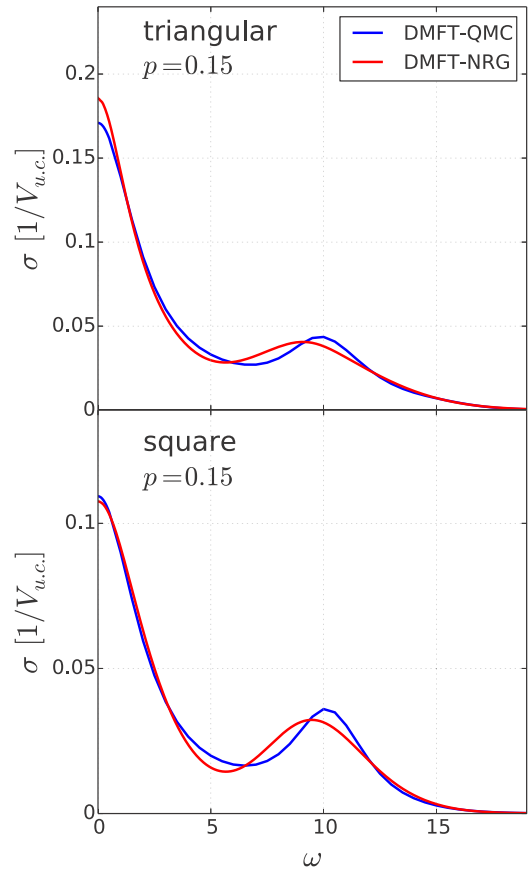

FIG. 9. DMFT-QMC and DMFT-NRG optical conductivity at $T = 1.4$.

observe $\rho \propto T^2$ behavior up to much lower temperatures on the square lattice. In this case, $\rho \propto T^2$ region is hardly visible on the scale of the plot, while $\rho \propto T^2$ up to $T \sim 0.3t$ on the triangular lattice. This observation is in agreement with the extension of the $C \propto T$ region in $C(T)$, which is restricted to lower temperatures in the case of a square lattice (Fig. 4).

A comparison of the DMFT-NRG (red lines) and DMFT-QMC (blue lines) optical conductivity at $T = 1.4t$ is shown in Fig. 9. The overall agreement is very good. We, however, find a small discrepancy at $\omega \sim 10t$. The DMFT-QMC result has the Hubbard peak in $\sigma(\omega)$ centered exactly at $\omega = U$, whereas it is shifted to slightly lower frequency in the DMFT-NRG solution. This shift is an artifact of numerical approximations in DMFT-NRG. A position of the Hubbard peak at $U = 10t$ is another manifestation of the precision of analytical continuation of the QMC data.

APPENDIX B: FINITE-SIZE EFFECTS IN CHARGE SUSCEPTIBILITY

In Fig. 10 we show the charge susceptibility obtained with different methods. The single-site DMFT result agrees very well with the 4×4 FTLM after averaging over the twisted boundary conditions. We show χ_c averaged over $N_{\text{tbc}} = 1$, 4, 16, 64, and 128 clusters with different boundary conditions. χ_c obtained with a single setup of boundary conditions deviates at low temperatures from the averaged values. The DCA results for $T \lesssim 0.5t$ are also inconsistent.
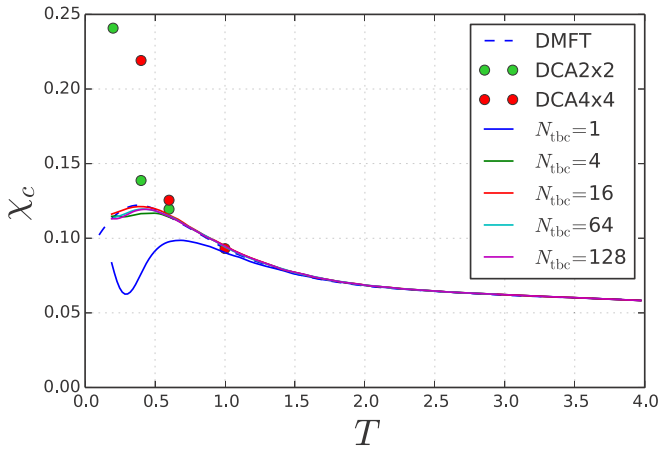
FIG. 10. Charge susceptibility as a function of temperature for the triangular lattice at $p = 0.15$ hole doping.

We believe that this is an artifact of the particular choice of the Brillouin zone patches. In DCA 4×4 and 2×2 we have just four and two independent patches in the Brillouin zone for triangular lattice, respectively.

APPENDIX C: DMFT DENSITY OF STATES

Here, we illustrate the density of states in different transport regimes in the DMFT solution. The results in Fig. 11 are obtained with the QMC solver followed by the Padé analytical continuation. We have checked that the density of states agrees with the DMFT-NRG result.

In the Fermi-liquid regime at low temperatures there is a peak in the density of states around the Fermi level. In the doped case the coherence-decoherence crossover is at temperature $T \sim 0.3$, as we established from the specific-heat data (see Fig. 4) and from the condition that the resistivity reaches the Mott-Ioffe-Regel limit (see Sec. III B). In agreement with earlier work [10,12], we see that at $T \sim 0.3$ there is a peak in the density of states even though long-lived quasiparticles are absent. At even higher temperatures (here shown $T = 1.4$), deeply in the bad-metal regime, the peak at the density of states at the Fermi level is completely washed out.
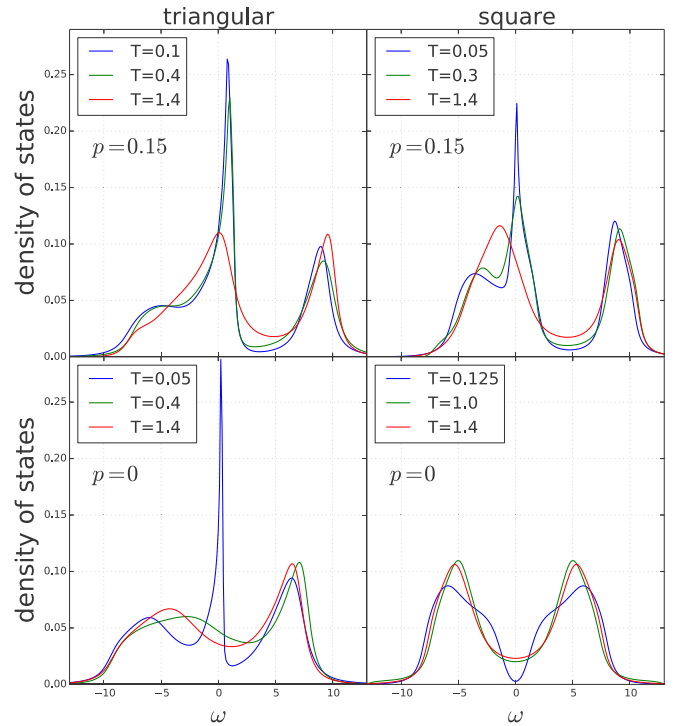

FIG. 11. Density of states in the Fermi liquid at low temperatures and in the bad-metal regime at high temperatures.

At half-filling the result is very sensitive to the exact position of parameters on the U-T phase diagram (see Fig. 2). For the triangular lattice at $U = 10$ the solution is metallic even at low temperature which leads to the formation of narrow quasiparticle peak at the Fermi level. This peak is quickly suppressed by thermal fluctuations which is accompanied by a sudden increase in the resistivity. For the square lattice at $U = 10$ the system is insulating above for $T \gtrsim 0.03$, while the Mott gap gradually gets filled as the temperature increases. We note that the low-temperature peak in optical conductivity in Fig. 7 is not connected to the existence of quasiparticles. It is just a consequence of a finite spectral density at the Fermi level (the absence of an energy gap), as expected in the bad-metal regime.

[1] S. A. Kivelson, I. P. Bindloss, E. Fradkin, V. Oganesyan, J. M. Tranquada, A. Kapitulnik, and C. Howald, Rev. Mod. Phys. **75**, 1201 (2003).

[2] B. J. Powell and R. H. McKenzie, Rep. Prog. Phys. **74**, 056501 (2011).

[3] K. Miyagawa, A. Kawamoto, Y. Nakazawa, and K. Kanoda, Phys. Rev. Lett. **75**, 1174 (1995).

[4] Y. Shimizu, K. Miyagawa, K. Kanoda, M. Maesato, and G. Saito, Phys. Rev. Lett. **91**, 107001 (2003).

[5] V. Dobrosavljević, N. Trivedi, and J. M. Valles, Jr., *Conductor-Insulator Quantum Phase Transitions* (Oxford University Press, Oxford, 2012).

[6] O. Gunnarsson, M. Calandra, and J. E. Han, Rev. Mod. Phys. **75**, 1085 (2003).

[7] N. E. Hussey, K. Takenaka, and H. Takagi, Philos. Mag. **84**, 2847 (2004).

[8] M. M. Qazilbash, K. S. Burch, D. Whisler, D. Shrekenhamer, B. G. Chae, H. T. Kim, and D. N. Basov, Phys. Rev. B **74**, 205118 (2006).

[9] M. M. Qazilbash, J. J. Hamlin, R. E. Baumbach, L. Zhang, D. J. Singh, M. B. Maple, and D. N. Basov, Nat. Phys. **5**, 647 (2009).

[10] X. Deng, J. Mravlje, R. Žitko, M. Ferrero, G. Kotliar, and A. Georges, Phys. Rev. Lett. **110**, 086401 (2013).

[11] W. Xu, K. Haule, and G. Kotliar, Phys. Rev. Lett. **111**, 036401 (2013).

[12] J. Vučičević, D. Tanasković, M. J. Rozenberg, and V. Dobrosavljević, Phys. Rev. Lett. **114**, 246402 (2015).

[13] H. Terletska, J. Vučičević, D. Tanasković, and V. Dobrosavljević, Phys. Rev. Lett. **107**, 026401 (2011).

[14] J. Vučičević, H. Terletska, D. Tanasković, and V. Dobrosavljević, Phys. Rev. B **88**, 075143 (2013).

[15] T. Furukawa, K. Miyagawa, H. Taniguchi, R. Kato, and K. Kanoda, Nat. Phys. **11**, 221 (2015).

[16] H. Eisenlohr, S.-S. B. Lee, and M. Vojta, Phys. Rev. B **100**, 155152 (2019).

[17] B. H. Moon, G. H. Han, M. M. Radonjić, H. Ji, and V. Dobrosavljević, arXiv:1911.02772.

[18] J. Kokalj, Phys. Rev. B **95**, 041110(R) (2017).

[19] E. W. Huang, R. Sheppard, B. Moritz, and T. P. Devereaux, Science **366**, 987 (2019).

[20] E. Perepelitsky, A. Galatas, J. Mravlje, R. Žitko, E. Khatami, B. S. Shastry, and A. Georges, Phys. Rev. B **94**, 235115 (2016).

[21] S. Hartnoll, Nat. Phys. **11**, 54 (2015).

[22] S. A. Hartnoll, A. Lucas, and S. Sachdev, *Holographic Quantum Matter* (MIT Press, Cambridge, MA, 2018).

[23] P. Cha, A. A. Patel, E. Gull, and E.-A. Kim, arXiv:1910.07530.

[24] P. T. Brown, D. Mitra, E. Guardado-Sanchez, R. Nourafkan, A. Reymbaut, C.-D. Hébert, S. Bergeron, A.-M. S. Tremblay, J. Kokalj, D. A. Huse, P. Schauß, and W. S. Bakr, Science **363**, 379 (2019).

[25] J. Vučičević, J. Kokalj, R. Žitko, N. Wentzell, D. Tanasković, and J. Mravlje, Phys. Rev. Lett. **123**, 036601 (2019).

[26] A. Georges, G. Kotliar, W. Krauth, and M. J. Rozenberg, Rev. Mod. Phys. **68**, 13 (1996).

[27] T. A. Maier, M. Jarrell, T. Prushke, and M. H. Hettler, Rev. Mod. Phys. **77**, 1027 (2005).

[28] J. Jaklič and P. Prelovšek, Adv. Phys. **49**, 1 (2000).

[29] N. Lin, E. Gull, and A. J. Millis, Phys. Rev. B **80**, 161105(R) (2009).

[30] N. Lin, E. Gull, and A. J. Millis, Phys. Rev. B **82**, 045104 (2010).

[31] D. Bergeron, V. Hankevych, B. Kyung, and A.-M. S. Tremblay, Phys. Rev. B **84**, 085128 (2011).

[32] T. Sato, K. Hattori, and H. Tsunetsugu, Phys. Rev. B **86**, 235137 (2012).

[33] T. Sato and H. Tsunetsugu, Phys. Rev. B **94**, 085110 (2016).

[34] A. Kauch, P. Pudleiner, K. Astleithner, P. Thunström, T. Ribic, and K. Held, Phys. Rev. Lett. **124**, 047401 (2020).

[35] A. Georges, Ann. Phys. (Berlin) **523**, 672 (2011).

[36] K. Aryanpour, W. E. Pickett, and R. T. Scalettar, Phys. Rev. B **74**, 085117 (2006).

[37] G. Li, A. E. Antipov, A. N. Rubtsov, S. Kirchner, and W. Hanke, Phys. Rev. B **89**, 161118(R) (2014).

[38] G. Kotliar, S. Y. Savrasov, G. Pálsson, and G. Biroli, Phys. Rev. Lett. **87**, 186401 (2001).

[39] G. Biroli and G. Kotliar, Phys. Rev. B **65**, 155112 (2002).

[40] A. N. Rubtsov and A. I. Lichtenstein, J. Exp. Theor. Phys. Lett. **80**, 61 (2004).

[41] E. Gull, A. J. Millis, A. I. Lichtenstein, A. N. Rubtsov, M. Troyer, and P. Werner, Rev. Mod. Phys. **83**, 349 (2011).

[42] K. G. Wilson, Rev. Mod. Phys. **47**, 773 (1975).

[43] H. R. Krishna-murthy, J. W. Wilkins, and K. G. Wilson, Phys. Rev. B **21**, 1003 (1980).

[44] R. Bulla, T. A. Costi, and T. Pruschke, Rev. Mod. Phys. **80**, 395 (2008).

[45] R. Žitko and T. Pruschke, Phys. Rev. B **79**, 085106 (2009).

[46] H. T. Dang, X. Y. Xu, K.-S. Chen, Z. Y. Meng, and S. Wessel, Phys. Rev. B **91**, 155101 (2015).

[47] H. Park, K. Haule, and G. Kotliar, Phys. Rev. Lett. **101**, 186403 (2008).

[48] H. Lee, G. Li, and H. Monien, Phys. Rev. B **78**, 205117 (2008).

[49] T. Shirakawa, T. Tohyama, J. Kokalj, S. Sota, and S. Yunoki, Phys. Rev. B **96**, 205130 (2017).

[50] J. Merino, B. J. Powell, and R. H. McKenzie, Phys. Rev. B **73**, 235107 (2006).

[51] J. Kokalj and R. H. McKenzie, Phys. Rev. Lett. **110**, 206402 (2013).

[52] T. Schäfer, F. Geles, D. Rost, G. Rohringer, E. Arrigoni, K. Held, N. Blümer, M. Aichhorn, and A. Toschi, Phys. Rev. B **91**, 125109 (2015).

[53] E. G. C. P. van Loon, M. I. Katsnelson, and H. Hafermann, Phys. Rev. B **98**, 155117 (2018).

[54] C. Walsh, P. Sémon, D. Poulin, G. Sordi, and A.-M. S. Tremblay, Phys. Rev. B **99**, 075122 (2019).

[55] J. Bonča and P. Prelovšek, Phys. Rev. B **67**, 085103 (2003).

[56] J. Vučičević and M. Ferrero, Phys. Rev. B **101**, 075113 (2020).

[57] A. Taheridehkordi, S. H. Curnoe, and J. P. F. LeBlanc, Phys. Rev. B **99**, 035120 (2019).

[58] A. Taheridehkordi, S. H. Curnoe, and J. P. F. LeBlanc, Phys. Rev. B **101**, 125109 (2020).

[59] A. Taheridehkordi, S. H. Curnoe, and J. P. F. LeBlanc, Phys. Rev. B **102**, 045115 (2020).

[60] O. Parcollet, M. Ferrero, T. Ayral, H. Hafermann, P. Seth, and I. S. Krivenko, Comput. Phys. Commun. **196**, 398 (2015).

[61] R. Peters, T. Pruschke, and F. B. Anders, Phys. Rev. B **74**, 245114 (2006).

[62] A. Weichselbaum and J. von Delft, Phys. Rev. Lett. **99**, 076402 (2007).

[63] R. Žitko, Phys. Rev. B **84**, 085142 (2011).

[64] R. Žitko, D. Hansen, E. Perepelitsky, J. Mravlje, A. Georges, and B. S. Shastry, Phys. Rev. B **88**, 235132 (2013).

[65] H. Kajueter and G. Kotliar, Phys. Rev. Lett. **77**, 131 (1996).

[66] M. Potthoff, T. Wegner, and W. Nolting, Phys. Rev. B **55**, 16132 (1997).

[67] L.-F. Arsenault, P. Sémon, and A.-M. S. Tremblay, Phys. Rev. B **86**, 085133 (2012).

The role of driving signal in the evolution of social networks

Ana Vranić and Marija Mitrović Dankulov

Scientific Computing Laboratory, Center for Study of Complex Systems, Institute of Physics Belgrade, University of Belgrade, Pregrevica 118, 11080 Belgrade, Serbia

1   Introduction

Dynamics and emergence of collective behavior in social system strongly depend on the structure of the interactions between actors in the social network. The nature of connections has been studied through empirical analysis and theoretical models of evolving networks [1]. Models of evolving networks start with one, or the small number of randomly connected nodes. The network grows by the addition of new nodes, which link to ones already present in the system, following some linking rule. These rules can shape the network in a specific way. For example, the preferential attachment mechanism is essential for reproducing the networks with a heterogeneous distribution of the number of first neighbors.

The role of driving, i.e., non-constant addition of new nodes in the network is still poorly understood. While standard networks models assume that the addition of new nodes is constant in time, the growth signal of real social systems varies and influences network structure [2]. It is of great importance to understand the interplay between the driving signal and network topology, and how they, separately and in combination, shape the collective behaviour in social systems. We use a model of network with aging nodes to examine the role of driving signal in a network.

2   Results

The aging model incorporates the time in a non-trivial manner by introducing nodes aging [3]. The network is generated by adding one node with one link to the target node in each time step, t. Probability for connecting new node in the network depends on degree k of the target node and the age difference τ between the new and target node,

$$\Pi_i(t) \sim k_i(t)^\beta \tau_i^\alpha \tag{1}$$

Different values of parameters α and β lead to networks with different structural properties.

We customised the aging model by allowing the addition of multiple nodes $(M > 1)$ and links $(L > 1)$, in each time step. As input in the simulation, we used the driving signal from the Meetup website, TECH social group [4]. Driving signal shows the number of new members that joined a group at a single event.

We run the simulations for TECH signal and randomized TECH signal, for all combinations of parameters $-3 < \alpha < 0$ and $1 < \beta < 3$, generating a sample of 100 networks. New members in network can make one ($L = 1$), or more ($L = 3$) connections. As the average number of added nodes per time step is $M = 1$, we looked into differences of networks driven with original and randomized TECH signal and ones with constant growth in the time. We use dissimilarity measure (D-distance) [5] to compare samples of networks grown with different signals. D-distance considers Jensen-Shenon divergence and node distance distribution.
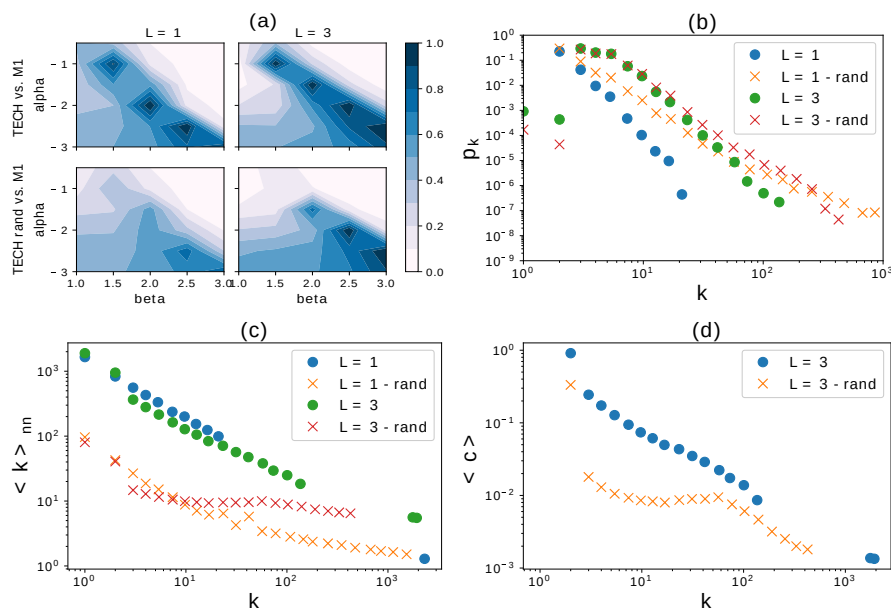

Fig. 1. (a) Dissimilarity distance between networks with (randomized) TECH and constant $M = 1$ signal, for number of links $L = 1$ and $L = 3$ in α-β plain. Network properties of (randomized) TECH signal for different values of L: (b) degree distribution, (c) dependence of average neighbor degree on node degree, (d) node clustering coefficient; for fixed model parameters $\alpha = -1$. and $\beta = 1.5$

Figure **1(a)** shows calculated D-distance between networks obtained for original driving signal vs. $M = 1$ (upper panel) and for randomized driving signal vs. $M = 1$ (lower panel). We notice a critical region around $\beta = 1.5$ and $\alpha = -1$, where D-distance between TECH and M1 signal is greater than between randomized TECH signal and M1. For these parameters, we represent the topological features of networks. For degree distribution (**Fig.1(b)**) we observe the only difference in slope between original and randomized TECH signal, with linking parameters $L = 1$ and $L = 3$. Networks generated with the original and reshuffled signal have significantly different topology if we compare degree-degree correlations and clustering coefficient.

Networks obtained for the real signals are strongly disassortative (**Fig.1(c)**) and have hierarchical structure, i.e., their clustering coefficient (**Fig.1(d)**) decreases with k. On the other hand, networks observed from driving the model with the randomized signal are uncorrelated, and their clustering weakly depends on the degree. Networks generated with the aging network model for L=1 are tree-like networks. They don't have triangles and their clustering is equal to 0.

Summary. Our results show that for the certain values of model parameters networks obtained from the driving with original signals have different topological features than ones obtained from the driving with random signals, although they evolve under the same linking rules. We find that driving signals alter the shape of the degree distribution, degree-degree correlations and clustering in the network. The effect is the largest for the values of model parameters for which we obtained networks with broad degree distribution. This difference disappears as we move away from these parameters. Our results strongly support the conclusion that driving signal is an important factor in the evolution of social networks and it has to be included, as a parameter, in modeling social systems.

References

1. Boccaletti S, Latora V, Moreno Y, Chavez M, Hwang DU, Complex networks: Structure and dynamics, Phys. Rep. 424, 175-308 (2006).
2. Mitrović Dankulov M, Melnik V, Tadić B:The dynamics of meaningful social interactions and the emergence of collective knowledge. Scientific Reports volume 5, Article number: 12197 (2015)
3. Basu Hajra K, Sen P.:Phase transitions in an aging network. Phys. Rev. E 70, 056103 (2004)
4. Smiljanić J, Mitrović Dankulov M: Associative nature of event participation dynamics: A network theory approach, PLoS ONE 12, e0171565 (2017)
5. Schieber et. all (2017).: Quantification of network structural dissimilarities. Nature Communications. 8. 13928. 10.1038/ncomms1392 (2017)

Collective social phenomena: physics perspective

Aleksandra Alorić, Ana Vranić, Marija Mitrović Dankulov, Jelena Smiljanić

Development and use of information communication technologies have enabled access to various types of data about human behavior. The availability of data is the main driving force behind the expansion of a new interdisciplinary field commonly known as computational social science [1]. The main goal of this new scientific discipline is to provide us with a quantitative description and understanding of complex social behavior. Researchers from different areas of science, including physics, computer science, mathematics, economics, and sociology, are making the best use of data and various computational techniques to achieve this goal. Statistical physics, in combinations with data analysis, theoretical modeling, and complex networks theory has proven to be very effective in uncovering and quantifying the mechanisms that underlie the collective behavior in social systems [1]. In this short overview of recent results we will demonstrate how techniques and methods of complex networks and statistical physics can provide a better understanding of the emergence of collective emotions in cyberspace [2] and cooperative long-term market loyalty in double auction markets [3], collective knowledge building [4] and dynamics of event-driven social groups [5].

[1] P. Sen, B.K. Chakrabarti, Sociophysics: An Introduction, Oxford University Press (2014).

[2] M. Mitrović, G. Paltoglou and B. Tadić, Quantitative analysis of bloggers' collective behavior powered by emotions, Journal of Statistical Mechanics: Theory and Experiment 2011, P02005 (2011)

[3] A. Alorić, P. Sollich, P. McBurney, and T. Galla: Emergence of Cooperative Long-Term Market Loyalty in Double Auction Markets, PLoS ONE 11, e0154606 (2016).

[4] M. Mitrović Dankulov, R. Melnik and B. Tadić, The dynamics of meaningful social interactions and the emergence of collective knowledge, Scientific Reports 5, 12197 (2015).

[5] J. Smiljanić and M. Mitrović Dankulov, Associative nature of event participation dynamics: A network theory approach, PLoS ONE 12, e0171565 (2017)

In Session 3*: Social Media and Big Data in Transport Analysis and Planning*

- **Ms. Maria Karatsoli**, University of Thessaly, Greece:
  Intelligent transport systems with usage of "big data" for management of sustainable mobility

- **Ms. Rosa Arroyo**, Universitat Politecnica de Valencia, Spain*:*
  Influence of attitudes towards the use of ICT Social Network in mobility and social interactions on commuting trips

- ❖ **Young researchers' Posters Session** (by alphabetic order) **in COST TU1305 Final Conference:**

1. **Mr. Adam Arnaud**, *Rediscovering urban models with non -conventional data and methods? The mosaic of Brussels.* Catholic University of Louvain-la-Neuve, Belgium.

2. **Mr. Aschauer Florian***, The changing character of travel behaviour: An innovative survey design for understanding individuals' trade-off processes.* Institute for Transport Studies, University of Natural Resources and Life Sciences, Vienna, Austria.

3. **Mr. Ding Ma***, A Smooth Curve as a Fractal Under the Third Definition*. University of Gävle, Sweden.

4. **Mr. Hanchard Matthew***, Latent resources and spatial practice: if mobile media are not directly used, can they still inform mobilities?* Newcastle University, UK.

5. **Mr. Karakikes Ioannis**, *Evaluation of Social Delivery as key-measure to last mile distribution.* University of Thessaly, Greece.

6. **Mr. Khoury Sabri***, Virtual Mental Maps*. Faculty of Architecture and town planning, Technion, Israel.

7. **Mr. Rubinstein Yuval***, Dynamic Urban Planning. Developing a dynamic urban planning model based on advance information systems*. Faculty of Architecture and town planning, Technion, Israel.

8. **Mr. Soler Daniel Casquero***, Influence of attitudes towards the use of ICT Social Networks in mobility and social interactions on leisure travel behavior.* Universitat Politecnica de Valencia, Spain.

9. **Ms. Vranic Ana***, Social network structure: physics perspective*. Institute of Physics in Belgrade, Serbia.

THE INFLUENCE OF LONG-RANGE CORRELATED GROWTH SIGNALSON THE EVOLVING COMPLEX NETWORK STRUCTURES

Ana Vranić, Marija Mitrović Dankulov

University of Belgrade, Institute of Physics Belgrade, Belgrade, Serbia

Summary: The application of wireless sensor networks (WSN) grows by the day. It is not surprising that methods for the design of energy-efficient and resilient WSN are one of the critical tasks for scientists working in this field. Complex network theory provides methods for studying and designing WSN. Models of complex networks are an efficient tool for uncovering mechanisms that can lead to networks with desired structural and dynamical properties. The main ingredients of a network model are growth and linking rules. The connection between linking rules and emergent topologies of complex networks has been extensively studied. On the other hand, how the properties of growth signal influence the structure of generated networks is still unknown to a large extent. Here we explore how the temporal correlation in growth signals change the structure of the networks with ageing nodes. We find that scale-free networks grown with time-varying signals have different global and local properties compared to ones grown with the constant signal. Signals with long-range correlations change the structure of the networks more than signals similar to white noise. Our results imply that growth signals and their properties need to be considered in the modelling of real complex networks, including WSN.

Keywords: complex networks, complex networks models, time-varying growthsignals

Република Србија
Универзитет у Београду
Физички факултет
Д.Бр.2017/8006
Датум: 22.04.2021. године

На основу члана 161 Закона о општем управном поступку и службене евиденције издаје се

УВЕРЕЊЕ

Вранић (Миладин) Ана, бр. индекса 2017/8006, рођена 23.11.1993. године, Чачак, Република Србија, уписана школске 2020/2021. године, у статусу: самофинансирање; тип студија: докторске академске студије; студијски програм: Физика.

Према Статуту факултета студије трају (број година): три.
Рок за завршетак студија: у двоструком трајању студија.

Ово се уверење може употребити за регулисање војне обавезе, издавање визе, права на дечији додатак, породичне пензије, инвалидског додатка, добијања здравствене књижице, легитимације за повлашћену вожњу и стипендије.

Овлашћено лице факултета

Република Србија
Универзитет у Београду
Физички факултет
Број индекса: 2017/8006
Датум: 22.04.2021.

На основу члана 29. Закона о општем управном поступку и службене евиденције издаје се

УВЕРЕЊЕ О ПОЛОЖЕНИМ ИСПИТИМА

Ана Вранић, име једног родитеља Миладин, рођена 23.11.1993. године, Чачак, Република Србија, уписана школске 2017/2018. године на докторске академске студије, школске 2020/2021. године уписана на статус самофинансирање, студијски програм Физика, током студија положила је испите из следећих предмета:

Р.бр.	Шифра	Назив предмета	Оцена	ЕСПБ	Фонд часова**	Датум
1.	ДС15КМ11	Физика фазних прелаза	10 (десет)	15	I:(8+0+0)	09.02.2018.
2.	ДС15КМ5	Физика неуређених система	10 (десет)	15	II:(8+0+0)	11.07.2017.
3.	ДС15ФРНД1	Рад на докторату 1. део	П.	30	I:(0+0+12) II:(0+0+12)	
4.	ДС15КМ4	Неравнотежна статистичка физика	10 (десет)	15	III:(8+0+0)	22.01.2019.
5.	ДС15ФРНД2	Рад на докторату 2. део	П.	30	III:(0+0+12) IV:(0+0+12)	
6.	ДС15ВО2	Монте Карло симулације у физици	10 (десет)	15	III:(8+0+0)	13.09.2019.
7.	ДС15ФРНД4	Рад на докторату 4. део	П.	15	V:(0+0+20)	
8.	ДС15ФРНД3	Рад на докторату 3. део	П.	15	V:(0+0+20)	

* - еквивалентиран/признат испит.

** - Фонд часова је у формату (предавања+вежбе+остало).

Општи успех: 10,00 (десет и 00/100) , по годинама студија (10,00, 10,00, /).

Овлашћено лице факултета

Универзитет у Београду
Физички факултет, Београд

Оснивач: Република Србија
Дозволу за рад број 612-00-02666/2010-04 од 10. децембра 2010.
године је издало Министарство просвете и науке Републике Србије

Диплома

Ана, Миладин, Вранић

рођена 23. новембра 1993. године у Чачку, Република Србија, уписана школске 2016/2017. године, а дана 27. септембра 2017. године завршила је мастер академске студије, другог степена, на студијском програму Теоријска и експериментална физика, обима 60 (шездесет) бодова ЕСПБ са просечном оценом 10,00 (десет и 0/100).

На основу тога издаје јој се ова диплома о стеченом високом образовању и академском називу

мастер физичар

Број: 8934700
У Београду, 28. новембра 2018. године

Декан
Проф. др Иван Белча

Ректор
Проф. др Иванка Поповић

Универзитет у Београду
Физички факултет, Београд

Оснивач: Република Србија

Дозволу за рад број 612-00-02666/2010-04 од 10. децембра 2010. године је издало Министарство просвете и науке Републике Србије

Диплома

Ана, Миладин, Вранић

рођена 23. новембра 1993. године у Чачку, Република Србија, уписана школске 2012/2013. године, а дана 22. јула 2016. године завршила је основне академске студије, првог степена, на студијском програму Теоријска и експериментална физика, обима 240 (двеста четрдесет) бодова ЕСПБ са просечном оценом 9,24 (девет и 24/100).

На основу тога издаје јој се ова диплома о стеченом високом образовању и стручном називу

дипломирани физичар

Број: 8595000

У Београду, 19. септембра 2018. године

Декан	Ректор
Проф. др Јаблан Дојчиловић	Проф. др Владимир Бумбаширевић

	ДОКТОРСКЕ СТУДИЈЕ		

ПРЕДЛОГ ТЕМЕ ДОКТОРСКЕ ДИСЕРТАЦИЈЕ
КОЛЕГИЈУМУ ДОКТОРСКИХ СТУДИЈА

Школска година
20_20_/20_21_

Подаци о студенту

Име **Ана**

Презиме **Вранић**

Број индекса **8006/2017**

Научна област дисертације

физика кондензоване материје и статистичка физика

Подаци о ментору докторске дисертације

Име **Марија**

Презиме **Митровић Данкулов**

Научна област **статистичка физика**

Звање **виши научни сарадник**

Институција **Институт за физику**

Предлог теме докторске дисертације

Наслов

Evolving complex networks: structure and dynamics

Растуће комплексне мреже: структура и динамика

Уз пријаву теме докторске дисертације Колегијуму докторских студија, потребно је приложити
следећа документа:

1. Семинарски рад (дужине до 10 страница)
2. Кратку стручну биографију писану у трећем лицу једнине
3. Фотокопију индекса са докторских студија

Потпис ментора _Марија Митровић Данкулов_

Датум 17. 02. 2021.

Потпис студента _Ана Врањић_

Мишљење Колегијума докторских студија

Након образложења теме докторске дисертације Колегијум докторских студија је тему

прихватио [✓] није прихватио [ ]

Датум

14. 04. 2021.

Продекан за науку Физичког факултета

[потпис]